

EMBRY-RIDDLE

Aeronautical University™

SCHOLARLY COMMONS

Dissertations and Theses

Spring 2013

A Preliminary Study of Acoustic Prediction Technology Based on Detached Eddy Simulations for Supersonic Jets Impinging on Flat Plates

Yuvraj Dewan

Embry-Riddle Aeronautical University - Daytona Beach

Follow this and additional works at: <https://commons.erau.edu/edt>



Part of the [Aerospace Engineering Commons](#)

Scholarly Commons Citation

Dewan, Yuvraj, "A Preliminary Study of Acoustic Prediction Technology Based on Detached Eddy Simulations for Supersonic Jets Impinging on Flat Plates" (2013). *Dissertations and Theses*. 45. <https://commons.erau.edu/edt/45>

This Thesis - Open Access is brought to you for free and open access by Scholarly Commons. It has been accepted for inclusion in Dissertations and Theses by an authorized administrator of Scholarly Commons. For more information, please contact commons@erau.edu.

A PRELIMINARY STUDY OF ACOUSTIC PREDICTION TECHNOLOGY BASED ON
DETACHED EDDY SIMULATIONS FOR SUPERSONIC JETS IMPINGING ON FLAT
PLATES

A Thesis
by
YUVRAJ DEWAN

Submitted to the Office of Graduate Studies of
Embry-Riddle Aeronautical University
in Partial Fulfillment of the Requirements for the Degree of
Master of Science

Spring 2013

Major Subject: Aerospace Engineering

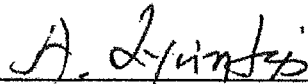
Copyright by Yuvraj Dewan 2013
All Rights Reserved

**A PRELIMINARY STUDY OF ACOUSTIC PREDICTION TECHNOLOGY BASED
ON
DETACHED EDDY SIMULATIONS FOR SUPERSONIC JETS IMPINGING ON
FLAT PLATES**

by
YUVRAJ DEWAN

This thesis was prepared under the direction of the candidate's thesis committee chairman Dr. Lyrintzis, Department of Aerospace Engineering, and has been approved by the members of his thesis committee. It was submitted to the Aerospace Engineering Department and accepted in partial fulfillment of the requirements of the degree of Master of Science in Aerospace Engineering.

THESIS COMMITTEE:



Dr. Anastasios Lyrintzis

Chair




Dr. Vladimir Golubev

Member



Dr. Konstantin Kurbatskii

Member



Dr. Reda Mankbadi

Member



Dr. Robert Oxley

Associate Vice President of Academics

3-5-2014

Date

Acknowledgements

This project was carried out with support from the United Launch Alliance and the Florida Center for Advanced Aero-Propulsion.

I would like to thank Dr. Lyrintzis, Dr. Golubev and Dr. Mankbadi at Embry-Riddle Aeronautical University (ERAU) for giving me the opportunity to work on this interesting project. The technical expertise and encouragement received from them made this work possible. I would also like to thank Dr. Konstantin Kurbatskii at ANSYS Inc. for his continuous assistance using the commercial code ANSYS FLUENT.

Next, I would like to express my gratitude to Lap Nguyen at ERAU for his assistance in matters dealing with the computing cluster used. I would also like to thank Kurt Aikens at Purdue University for his continued insight into the world of aeroacoustics and Large Eddy Simulation. Next, I recognize Barrett Guenthoer at ERAU for providing me with knowledge about the functioning of the FW-H methods.

Additionally, I would like to thank all my friends for their constant encouragement. This especially includes everyone working in the Computational Propulsion and Aerodynamics Laboratory at ERAU – Shibhani Bhatt, Miraj Desai, Nikisha Nagappan, Jonathan Nutzati.

Finally, I would like to thank my parents and family for their never-ending moral support, which has made my academic experience a very enjoyable one.

Nomenclature

General

f	Frequency
d_t	Throat diameter
d_e	Exit diameter
St	Strouhal number
V	Velocity
M	Mach number
p	Static pressure

Greek Symbols

ω	Angular frequency
λ	Wavelength
γ	Specific heat ratio
ρ	Static density

Acronyms

DDES	Delayed detached eddy simulation
DNS	Direct numerical simulation
FW-H	Ffowcs-Williams and Hawkings
LES	Large eddy simulation
RANS	Reynolds averaged Navier Stokes

Abstract

An application of an existing industry tool to study supersonic jets impinging on flat plates is shown. This industry tool is the commercially available CFD package ANSYS FLUENT. The supersonic jet studied is perfectly expanded with a Mach number of 1.5, and it impinges on a flat surface 4 nozzle throat diameters from the jet exit. All turbulence modeling is done using a hybrid RANS/LES technique known as Delayed Detached Eddy Simulation (DDES). A transient solution is calculated using the pressure-based coupled solver formulation with the second-order bounded central-upwind spatial discretization and second-order implicit time marching scheme. Flow features like the stagnation bubble, wall jet and feedback mechanism were studied using contour plots. An examination was also done into the mean flow fields of the jet core. The acoustics of the case were studied using two different techniques, direct measurement and the use of a acoustics source surface method. Using limited computational power, reasonable agreement between simulation and experimental data was found for the flow-field and acoustics. Thus, it was demonstrated that ANSYS FLUENT can be used for this problem to provide good preliminary results in an industry setting with limited computational power.

Contents

1	Introduction	1
1.1	Motivation	1
1.2	Sources of Jet Noise	2
1.2.1	Mixing Noise	3
1.2.2	Mach Noise	3
1.2.3	Screech Noise	3
1.2.4	Miscellaneous Noise	3
1.3	Flow Mechanisms	4
1.4	Previous Work	4
1.5	Benchmark Experiment	5
1.6	Thesis Objectives	6
1.7	Thesis Organization	6
2	Numerical Setup	9
2.1	Delayed Detached Eddy Simulation	9
2.2	Pressure-Based Coupled Solver	11
2.3	Time Marching	12
2.4	Solution Initialization	12
2.5	Computational Mesh	13
2.5.1	DDES Requirements	15
2.5.2	Acoustics Requirements	15
2.5.3	Azimuthal Requirements	16
2.6	Physical models and Boundary Conditions	17
2.7	Ffowes Williams-Hawkings Acoustics Integral Surface	18
2.8	Acoustics Post-Processing	21
3	Results	22
3.1	Flow Behavior	22

3.2	Mean Flow Field	35
3.3	Acoustics	38
3.3.1	Sound Source Identification	38
3.3.2	Feedback Mechanism	38
3.3.3	Near-Field Measurements	40
3.3.4	Effect of quarter vs full nozzle mesh	43
3.3.5	Ffowcs-Williams & Hawkings Results	44
3.3.6	Directivity	48
4	Conclusions and Future Work	51

List of Figures

1.1	The F-35 Joint Strike Fighter taking off from an aircraft carrier	1
1.2	A jet blast deflector being used on an aircraft carrier	2
1.3	Nozzle geometry	7
1.4	Schematic of benchmark experiment[6]	8
2.1	The near-field region of the computational mesh	13
2.2	The far-field of the computational mesh	14
2.3	Location of FW-H Surface	21
3.1	Static pressure contours after full multi-grid initialization	23
3.2	Mach number contours after full multi-grid initialization	24
3.3	Static temperature contours after full multi-grid initialization	25
3.4	TKE contours after full multi-grid initialization	26
3.5	Static pressure contours after RANS simulation	27
3.6	Mach number contours after RANS simulation	28
3.7	Static temperature contours after RANS simulation	29
3.8	TKE contours after RANS simulation	30
3.9	Static pressure contours after DDES simulation	31
3.10	Mach number contours after DDES simulation	32
3.11	Static temperature contours after DDES simulation	33
3.12	TKE contours after DDES simulation	34
3.13	Instantaneous Mach number contours. Each successive figure represents the next time step	36
3.14	Centerline Velocity of the Jet	37
3.15	Instantaneous vorticity magnitude contour plot	39
3.16	Normalized pressure contours demonstrating development of the feedback mechanism	40
3.17	Instantaneous Normalized Pressure Contours. Each successive figure repre- sents the next time step.	42

3.18	Comparison of simulation SPL data with experiment	43
3.19	Comparison of simulation SPL data with experiment using the direct propagation method (360° mesh)	44
3.20	Comparison of simulation SPL data with experiment calculated using the FWH source surface	45
3.21	Comparison of simulation SPL data with experimental data on doubling acoustic pressure history calculated on symmetry plane	46
3.22	Comparison of simulation SPL data with experimental data with microphone location between both symmetry planes	47
3.23	Comparison of simulation SPL data from both microphone location cases . .	48
3.24	Angle calculation for directivity	49
3.25	Directivity of the sound produced	50

Chapter 1

Introduction

1.1 Motivation

The study of the acoustics of supersonic jet impingement is one of great practical value. One of the primary reasons is the increased use of short take off and vertical landing (STOVL) aircraft. STOVL aircraft rely on directing the jets directly onto a flat surface during landing conditions as seen in Figure 1.1. This impingement can be a significant noise source leading to detrimental hearing conditions for the crew and the potential for the aircraft to be discovered. This problem is made more acute by the fact that most VTOL aircraft are operated on aircraft carriers since the close proximity of the onboard crew imposes additional noise limitations.



Figure 1.1: The F-35 Joint Strike Fighter taking off from an aircraft carrier

In certain conditions, conventional (non-VTOL) jet aircrafts need to be operated using

a jet blast deflector. A jet blast deflector is a device that redirects the jet exhaust away from operating crews and other critical equipment. Figure 1.2 shows a jet blast deflector in operation. The operation of this jet blast deflector is another situation in which jet impingement noise becomes a major concern.



Figure 1.2: A jet blast deflector being used on an aircraft carrier

The acoustic waves generated due to the jet impingement are also important aside from their impact on noise levels. In the case of VTOL aircraft, the acoustic waves can propagate back and impact the underbelly of the aircraft. This can lead to sonic fatigue and structural damage of the weapons and other payload that is exposed to these waves.

The study of supersonic impinging jets is also applicable in the design and analysis of rocket nozzles. There is a potential for reflected pressure waves, of the exhaust off the launch pad, to cause structural damage to the rocket nozzle and the payload. The launch pad itself can also suffer extensive damage due to the nature of the exhaust impinging on it.

Given the importance of the problem, the development of an computational method of estimating the flow field and acoustics of a supersonic impinging jet is the next logical step. The main purpose of this study is to implement numerical models in computational aeroacoustics (CAA) to carry out this prediction.

1.2 Sources of Jet Noise

To understand the effect of impingement on the noise generation mechanism, it is important to briefly introduce the sources of jet noise. Jet noise can be broadly categorized as follows:

1.2.1 Mixing Noise

Mixing noise is caused due to the interaction between the jet flow and the ambient air. The nozzle lip at the jet exit causes a turbulent shear layer to form at this interaction area. The instability of this shear layer serves as the primary mechanism by which mixing noise is generated. Mixing noise is most predominant close to the jet exit and decays as the jet velocity decreases. In most cases, mixing noise accounts for the biggest source of jet noise.

1.2.2 Mach Noise

Mach noise is a source of jet noise found in supersonic jet flow. A Mach wave is a pressure disturbance that propagates with the local speed of sound. In supersonic flow, no information is propagated past the Mach wave. McLaughlin et al. [17, 18] showed that noise from Mach waves is dominated by large scale turbulent structures for high Reynolds number supersonic jets. Mach wave has a dominant direction close to the axis. However, as one moves away from the downstream region, the noise diminishes quickly [3].

1.2.3 Screech Noise

Imperfectly expanded supersonic jets have an additional source of noise called screech noise. According to Powell, the screech tones are caused due to a resonant feedback loop caused within the flow [22, 21]. The interaction of the shock cell structure of the jet and the shear layer causes certain acoustic disturbances to develop. Some of these disturbances propagate backwards through the flow and interact with the nozzle lip to further excite the shear layer. This feedback leads to the development of high-frequency noise known as screech tones. The study of screech noise is important since screech tones can lead to sonic fatigue failure [23].

The effect of screech tones on a supersonic impinging jet depends mainly on the distance between the nozzle exit and the impingement surface. If the distance is too small, the shock cell structure of the jet is not fully developed and screech tones are not produced. However, if the distance is large enough, screech tones might be generated.

1.2.4 Miscellaneous Noise

Aside from the above aerodynamically generated noise, there are other miscellaneous sources of jet noise. These include combustion noise and mechanical noise generated by moving components, e.g. fan, compressor, turbine etc.

1.3 Flow Mechanisms

The study of the acoustic mechanism of impinging jets was first studied in detail by Powell [?]. This study examines the acoustic effects of round under-expanded jets impinging on flat surfaces. It was found that the jet becomes oscillatory when the impingement surface is close to the jet exit. Powell also noted that the main source of acoustics is the generation of a feedback mechanism in the system, which in turn is due to the oscillatory nature of the system.

To understand the mechanism of this feedback loop, it is important to understand the generation of the shear layer created at the jet exit. This shear layer is generated at the exit of the nozzle due to the jet interacting with the nozzle lip. This shear layer contains inherent instabilities lead to the creation of small scale and large scale vortical structures.

The impingement of the jet on the solid surface creates a number of pressure fluctuations. These pressure fluctuations propagate back through the subsonic region outside the core of the jet and contact the nozzle exit lip. This interaction leads to a change in the shear layer structure of the jet, which in turn leads to a change in the pressure fluctuations at the impingement zone. Once the system settles down to a stable frequency, the jet starts to oscillate at that frequency. This also leads to the wall jet (jet parallel to the wall flowing away from the jet core) being excited at that frequency. Finally, this oscillation also affects the behavior of the shock which appears right before the stagnation bubble. This shock is known as the standoff shock. All of these frequency dependent mechanisms contribute to certain tones being generated. Capturing and studying these tones is the major aim of this study.

Krothapalli has conducted experimental and numerical research which lend additional credibility to the feedback loop hypothesis [11]. He numerically predicted the frequencies that are generated by an impinging rectangular supersonic jet using the feedback loop theory and validated the results using experiments. Powell et. al also found that additional acoustic tones are observed when the impinging plate size is small. These are attributed to the change in behavior of the oscillations of the standoff shock, normal to the jet.

1.4 Previous Work

The study of supersonic jet impingement has been the topic of a number of experimental and numerical studies. Ho and Nosseir experimentally studied high subsonic impinging jets. They noted the upstream propagation of the reflected pressure waves from the impinging surface and their interaction with the nozzle lip. They also concluded that the waves propagating

upstream had the same phase with the downstream structures that propagated as a result of the feedback. Tam and Ahuja [28] analytically the generation of these feedback tones. They hypothesized that the initial energy for the feedback was provided by the instability waves in the shear layer of the jet. These waves propagate downstream and result in pressure fluctuations on impingement. These pressure fluctuations travel upstream to re-excite the shear layer at the nozzle lip. Krothapalli [11] verified the analytical relations given by Tam and Ahuja by experiments on an under expanded rectangular supersonic jet. Erwin and Sinha [6] experimentally studied supersonic impinging jets using an LES code, CRAFT CFD®LES. They were effectively able to predict broadband noise levels using the the integral surface (FWH) method, but were unable to predict peaks associated with the impingement tones. Brown and Frendi [4] used the NASA Overflow 2 code to conduct detached eddy simulations of supersonic impinging jets. They were effectively able to capture both broadband levels and peaks within the data. Their DES grid consisted of approximately 80 million cells.

1.5 Benchmark Experiment

To demonstrate the use of the code in successfully simulating the impingement of supersonic jets, a benchmark experiment is used so that simulation results can be validated. The experiment was done at Florida State University by Krothapalli et al [12]. The experimental setup contains a converging diverging axisymmetric nozzle with a throat diameter of 2.54 cm and an exit diameter of 2.75 cm. The converging section of the nozzle is a third degree polynomial with a contraction ratio of approximately 5. The diverging section of the nozzle is straight walled with a divergence angle of 3 degrees. A schematic of the nozzle is shown in figure 1.3. The nozzle is mounted flush with a solid circular plate called the lift plate. The impingement surface is 4 throat diameters away from the nozzle exit. The jet exiting the nozzle is ideally expanded with a nozzle pressure ratio of 3.7. This nozzle pressure ratio is the ratio of the stagnation pressure in the nozzle to the ambient pressure. The jet is unheated with a stagnation temperature of 20°C. The microphone is placed 25 cm away in plane with the nozzle exit. A schematic of the entire experimental setup is shown in figure 1.4. The experimental documentation includes results about the sound pressure level and some mean flow parameters. The benchmark experiment setup at FSU has also been used for a number of acoustics mitigation studies, e.g. acoustic reduction using micro jets [13].

1.6 Thesis Objectives

The aim of this thesis is to study the behavior and acoustic field of supersonic jets impinging on flat plates as would be done in an industrial setting. These results will be compared to available experimental data for validation purposes. The norm in most industrial settings is to use a commercially available solver which included pre-processing and post-processing tools, and available support. For this reason, all cases for this thesis are run using the commercial CFD solver ANSYS FLUENT. Since computational resources are at a premium in industry, every effort is taken to minimize computational cost for the simulation. It is for this reason that a hybrid RANS/LES known as DDES is used for computation. This method combines the computational efficiency of RANS simulations with the accuracy of LES.

1.7 Thesis Organization

Chapter 2 describes the numerical techniques implemented in modeling the flow and estimating acoustics. Chapter 3 shows the results from the numerical studies and provides a comparison with the results of the benchmark experiment. Finally, chapter 4 details conclusions that can be inferred from the results. It also includes recommendations for future work that can be used to broaden the scope of the project. Some of the results presented in this thesis are also included in Reference [5].

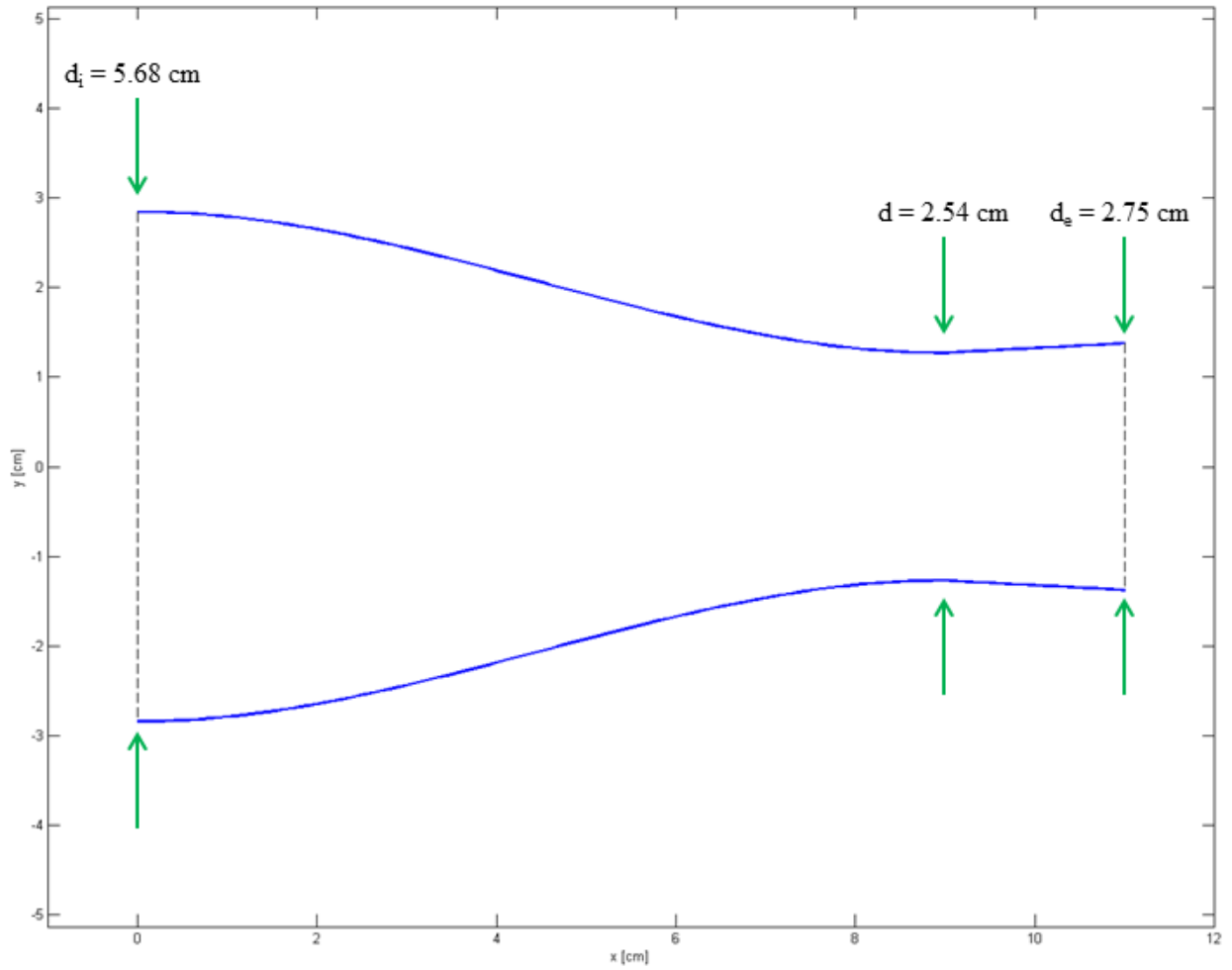


Figure 1.3: Nozzle geometry

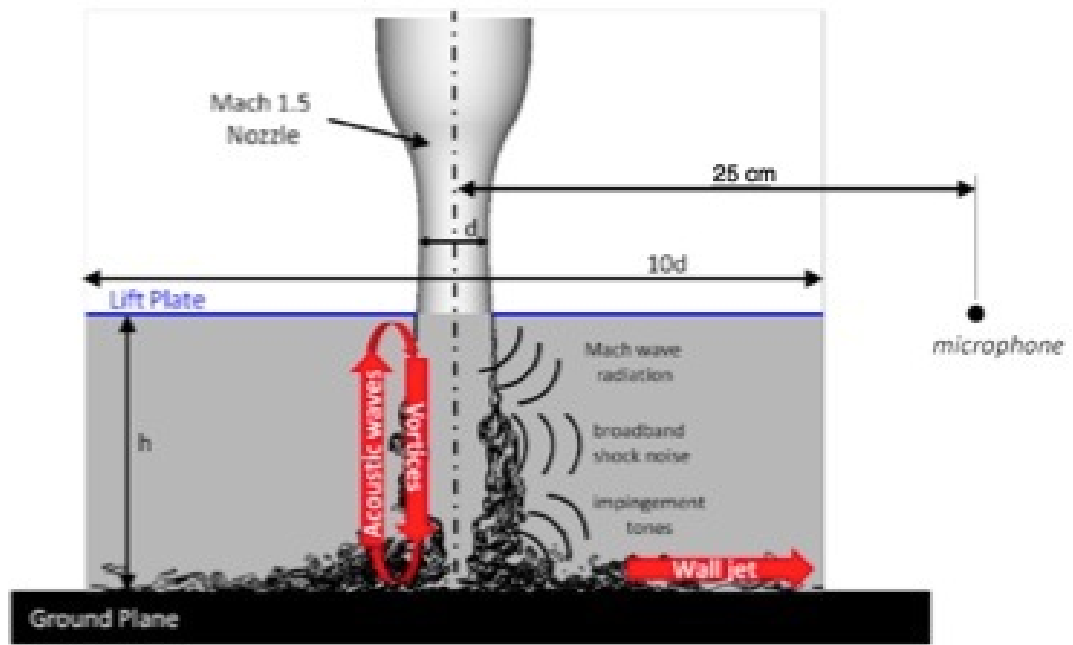


Figure 1.4: Schematic of benchmark experiment[6]

Chapter 2

Numerical Setup

ANSYS FLUENT solves the Navier-Stokes equations using the finite volume approach. The Navier-Stokes equations contain the continuity equation (equation 2.1), the three momentum equations (equations 2.2 to 2.4) and the energy equation 2.5.

$$\frac{\partial \rho}{\partial t} + \frac{\partial(\rho u)}{\partial x} + \frac{\partial(\rho v)}{\partial y} + \frac{\partial(\rho w)}{\partial z} = 0 \quad (2.1)$$

$$\frac{\partial(\rho u)}{\partial t} + \frac{\partial(\rho u^2)}{\partial x} + \frac{\partial(\rho uv)}{\partial y} + \frac{\partial(\rho uw)}{\partial z} = -\frac{\partial p}{\partial x} + \frac{1}{Re} \left[\frac{\partial \tau_{xx}}{\partial x} + \frac{\partial \tau_{xy}}{\partial y} + \frac{\partial \tau_{xz}}{\partial z} \right] \quad (2.2)$$

$$\frac{\partial(\rho v)}{\partial t} + \frac{\partial(\rho uv)}{\partial x} + \frac{\partial(\rho v^2)}{\partial y} + \frac{\partial(\rho vw)}{\partial z} = -\frac{\partial p}{\partial y} + \frac{1}{Re} \left[\frac{\partial \tau_{xy}}{\partial x} + \frac{\partial \tau_{yy}}{\partial y} + \frac{\partial \tau_{yz}}{\partial z} \right] \quad (2.3)$$

$$\frac{\partial(\rho w)}{\partial t} + \frac{\partial(\rho uw)}{\partial x} + \frac{\partial(\rho vw)}{\partial y} + \frac{\partial(\rho w^2)}{\partial z} = -\frac{\partial p}{\partial z} + \frac{1}{Re} \left[\frac{\partial \tau_{xz}}{\partial x} + \frac{\partial \tau_{yz}}{\partial y} + \frac{\partial \tau_{zz}}{\partial z} \right] \quad (2.4)$$

$$\begin{aligned} \frac{\partial E_T}{\partial t} + \frac{\partial(uE_T)}{\partial x} + \frac{\partial(vE_T)}{\partial y} + \frac{\partial(wE_T)}{\partial z} = & -\frac{\partial(up)}{\partial x} - \frac{\partial(vp)}{\partial y} - \frac{\partial(wp)}{\partial z} - \frac{1}{Re Pr} \left[\frac{\partial q_x}{\partial x} + \frac{\partial q_y}{\partial y} + \frac{\partial q_z}{\partial z} \right] \\ & + \frac{1}{Re} \left[\frac{\partial}{\partial x}(u\tau_{xx} + v\tau_{xy} + w\tau_{xz}) + \frac{\partial}{\partial y}(u\tau_{xy} + v\tau_{yy} + w\tau_{yz}) + \frac{\partial}{\partial z}(u\tau_{xz} + v\tau_{yz} + w\tau_{zz}) \right] \end{aligned} \quad (2.5)$$

2.1 Delayed Detached Eddy Simulation

Turbulence modeling is critical for computational aeroacoustics simulations since the small fluctuations in pressure must be captured accurately. There are a number of options for turbulence modeling such as RANS, LES and DNS simulations. Reynolds Averaged Navier-

Table 2.1: Common Turbulence Modeling Techniques

Technique	Large Scale Eddies	Small Scale Eddies
RANS	Modeled	Modeled
LES	Resolved	Modeled
DNS	Resolved	Resolved

Stokes (RANS) turbulence modeling is an approach in which all turbulent scales are modeled rather than resolved. Therefore, this type of model is not effective in simulating even simple shear flows. The next option is a Large Eddy Simulation (LES) in which all the large scales of turbulence are resolved while the smaller scales are modeled. The most accurate and computationally expensive simulation technique is known as Direct Numerical Simulation (DNS) in which all turbulence is directly resolved by the simulation. Table 2.1 summarizes the relationship between these three modeling techniques in relation to their treatment of turbulence. From a computational resource standpoint, LES and DNS are still too expensive to be used effectively in industry. The method of Detached Eddy Simulation (DES) combines the advantages of both RANS and LES methods by adopting a hybrid approach.

LES models are especially computationally expensive in areas of wall bounded flow. This is because the turbulence length scale becomes very small relative to the boundary layer thickness near the wall. The method of Detached Eddy Simulation [25, 26, 27] (DES) addresses this concern by switching to a RANS model in regions near walls and switching to an LES models in free shear flow regions. The switch between the RANS and LES solvers is purely a function of grid resolution (DES limiter) in different parts of the mesh. If the grid is fine enough to resolve the inertial scales of turbulence, the LES solver is applied to the region.

In some regions, the flow might not have sufficient turbulent content but the grid may be of LES resolution. This would lead to a situation where the LES formulation is activated without a proper generation of turbulent content, e.g. wall boundary layers. This may further lead to Grid-Induced Separation (GIS) [20] where the boundary layers separates at arbitrary locations based on the grid spacing. To counteract this, a modification of the DES to Delayed DES (DDES) is used which effectively 'shields' the boundary layer from the DES limiter [14]. Near field predictions are done using this DDES approach and far-field noise is calculated using the surface integral acoustic method know as the Ffowcs Williams-Hawkings (FW-H) method [7].

In regions where the RANS method is applied, the SST $k - \omega$ turbulence model is used. This model is a good fit for the simulation since it performs well under the conditions of wall

bounded flow within the nozzle, as well as the free shear flows. The SST $k - \omega$ model can be viewed as a fusion between the $k - \epsilon$ and the $k - \omega$ models. The $k - \omega$ model is applied in regions close to the wall while the $k - \epsilon$ model is applied in regions away from the wall.

2.2 Pressure-Based Coupled Solver

A pressure-based coupled solver is used in this study. Details about the implementation of the solver can be found in the FLUENT documentation [2]. Given the flow parameters, there are a number of key advantages to using this solver. Most high speed jet flows are numerically resolved using a density based couple formulation. In the density-based approach, density is used as a primary variable found from the continuity equation, and then pressure is deduced from it using an equation of state. The density-based approach is found to be efficient when used for high subsonic, transonic or supersonic flows. However, the disadvantage of a density-based coupled solver is that additional measures such as preconditioning[30, 31, 29] are required in regions where the flow becomes low subsonic, e.g. outside the jet. This pressure based solver has been used previously in similar jet simulations by one of the authors[14].

The coupled option was chosen for the solver since the inter-equation coupling in this system is large. A decoupled (segregated) solver solves the momentum equations and the pressure correction equations sequentially. However, a coupled solver solves a coupled system of equations comprising the momentum equations and the pressure equation. Due to this increased coupling between the equations, the rate of convergence is greatly increased.

The governing equations for the conservation of mass, momentum and energy are discretized using a control-volume-based technique. Face values required for computing the convection terms are interpolated from the cell centers using a bounded second-order central differencing of the variable. The implementation in ANSYS FLUENT [2] based on the normalized variable diagram (NVD) approach [15] together with the convection boundedness criterion (CBC). The bounded central differencing scheme is a composite NVD-scheme that consists of a pure central differencing, a blended scheme of the central differencing and the second-order upwind scheme, and the first-order upwind scheme. It should be noted that the first-order scheme is used only when the CBC is violated.

Gradients needed for constructing values of a scalar at the cell faces, and for computing secondary diffusion terms and velocity derivatives are calculated using the Green-Gauss node-based gradient evaluation [10]. In this approach, nodal values are constructed from the weighted average of the cell values surrounding the nodes, following the approach originally proposed by Holmes et al [8] and Rauch et al [24], and then gradients are computed at cell

centers by applying a discretized form of the Green-Gauss theorem. This scheme reconstructs exact values of a linear function at a node from surrounding cell-centered values on arbitrary unstructured meshes by solving a constrained minimization problem, preserving a second-order spatial accuracy.

An implicit discretization of the pressure gradient terms in the momentum equations, and an implicit discretization of the face mass flux, including the Rhie-Chow pressure dissipation terms, provide fully implicit coupling between the momentum and continuity equations. This discretization yields a system of algebraic equations whose matrix depends on the discretization coefficients of the momentum equations [2], and it is then solved using the coupled algebraic multigrid (AMG) scheme [2, 9]. An Incomplete Lower Upper (ILU) smoother is applied to smooth the residuals between levels of the AMG. The ILU smoother is more expensive than the standard Gauss-Seidel, but has better smoothing properties, especially for block-coupled systems solved by the coupled AMG, which permits more aggressive coarsening of AMG levels.

2.3 Time Marching

Time marching for the transient DDES run is done using a second order fully implicit solver. An implicit solver implies that a system of equations is solved at each time step through an iterative algorithm. The advantage of using a implicit scheme is that the solution is unconditionally stable. To reduce the computational time, the maximum number of iterations for each time step was set to be 10. The time step was chosen to be 2.5E-6 seconds. This was done to ensure that the frequency spectrum is being adequately resolved. Additionally, it was ensured that this time step was small enough to give consistent DDES results.

2.4 Solution Initialization

The solution was initialized in two steps. First, the full multi-grid (FMG) initialization was carried out followed by a RANS simulation. The FMG initialization clumps together neighboring cells to make a coarse mesh. The Euler equations are then solved on this mesh to provide an approximate solution for this coarse mesh. The mesh is then made finer by splitting and the Euler equations are solved again. This continues until the original grid is recovered with an initialized solution on it. It is important to note that the FMG solver does not resolve any turbulence. The RANS simulation is run after the FMG solver until reasonable convergence is seen in the solution.

2.5 Computational Mesh

Due to computational restrictions, only a quarter model of the nozzle was simulated. The computational mesh is created using a hybrid structured/unstructured technique. The mesh within the nozzle, the entire region $10d_t$ from the centerline is a structured hexahedral mesh. The remaining mesh, all the way to the far-field is an unstructured tetrahedral mesh. The mesh density is increased in the shear layer regions, as well as the region of impingement along the impingement surface, where the wall jet will develop. Figure 2.1 shows this inner region. The far-field is an unstructured tetrahedral mesh. This far-field region has a spherical boundary which is extremely far away from the near-field region. This far-field mesh is also highly stretched all the way to the boundary. The far-field mesh is designed with these characteristics to avoid any reflections from the boundary back into the domain, which can add inaccuracies to the results. Figure 2.2 shows this stretched far-field.

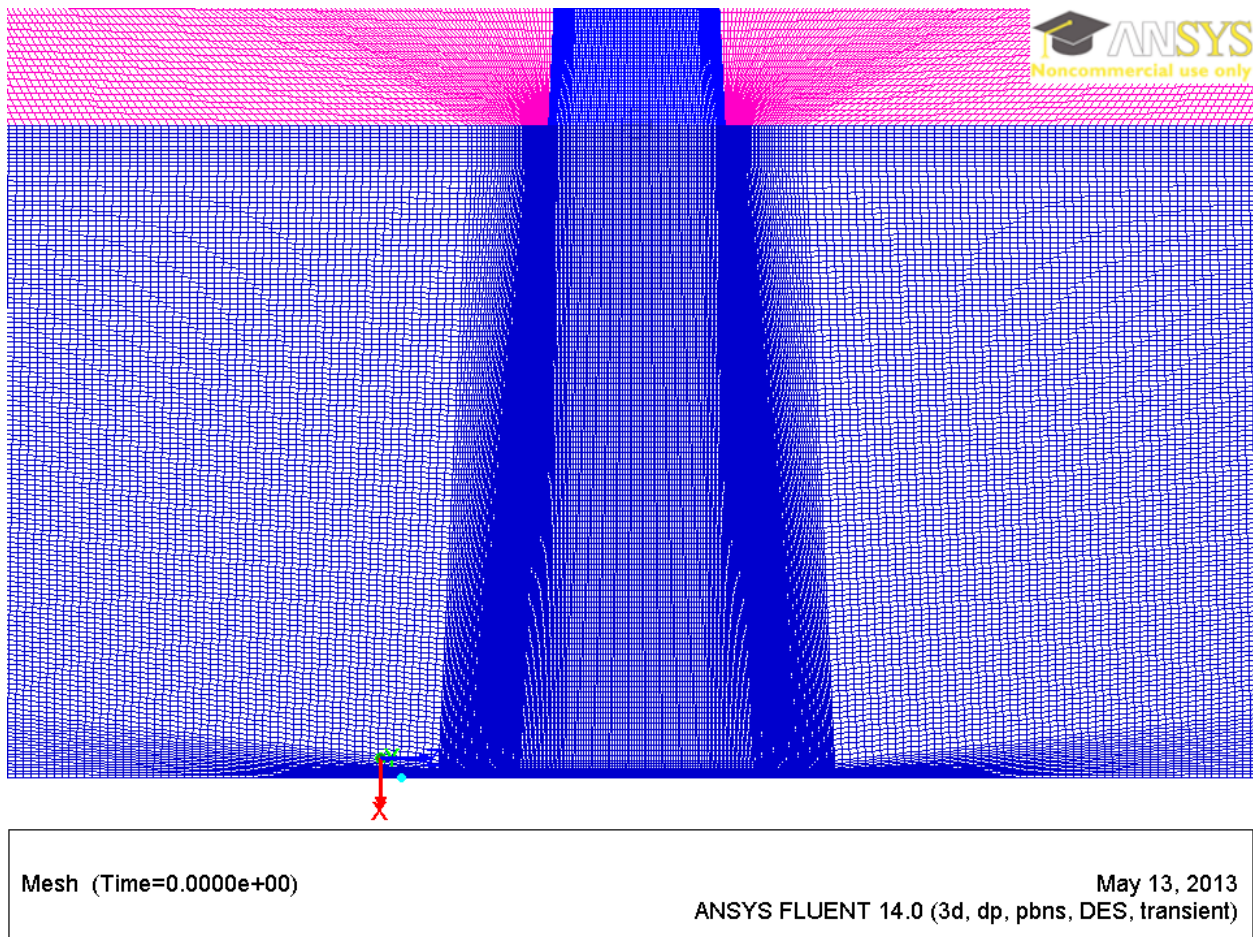


Figure 2.1: The near-field region of the computational mesh

Many considerations were taken into account when estimating mesh resolution in different

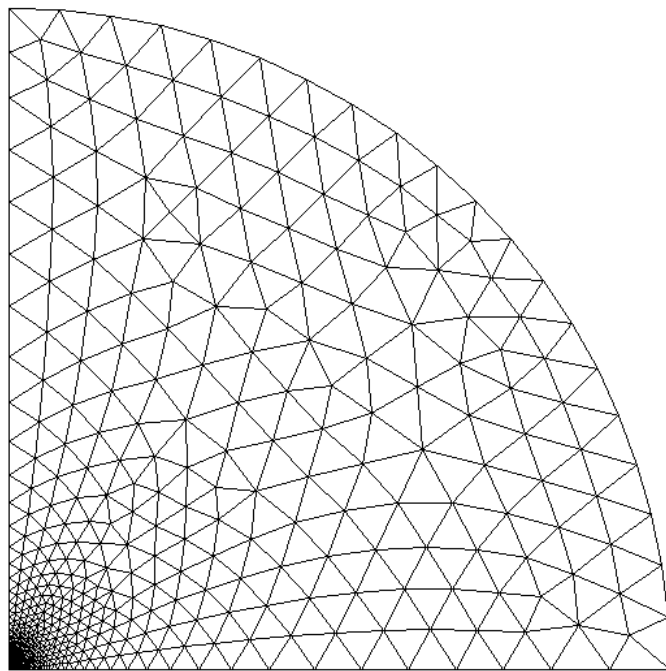


Figure 2.2: The far-field of the computational mesh

parts of the mesh. Table 2.2 contains the approximate mesh resolution in different directions in the near-field regions.

Table 2.2: Mesh resolution in each direction

Direction	Approximate Resolution
Axial (dx)	0.07857 cm
Radial (dr)	0.1258 cm
Azimuthal (dθ)	0.5541 cm

2.5.1 DDES Requirements

In certain regions next to the wall, it is important to resolve the boundary layer correctly. This is the case for the region where the wall jet starts to develop. In this region, the grid spacing is set for a y^+ of 1. For the shear layer region, the spacing is set to resolve the required length scales of turbulence.

2.5.2 Acoustics Requirements

The maximum Strouhal number (cutoff Strouhal number) that can be resolved by a mesh can be estimated by the mesh resolution up to the integral source surface. According to Aikens et al. [1], the mesh resolution for cutoff depends on a combination of the maximum resolution in the axial and radial direction. Therefore, for estimating the worst case scenario, the more restrictive radial mesh resolution of 0.1258 cm is used, as seen in table 2.2. Aikens et al. also explain that to accurately resolve a wavelength, 8 grid points must be used. Therefore, the minimum wavelength that can be estimated by the computational mesh is approximated by multiplying the grid length by 8, which results in a minimum wavelength of 1 cm. The maximum resolvable angular frequency can be estimated as shown.

$$\begin{aligned}
 a &= \lambda_{min} \omega_{max} \\
 \therefore \omega_{max} &= \frac{a}{\lambda_{min}} \\
 \therefore \omega_{max} &= \frac{340 \text{ m/s}}{0.01 \text{ m}} \\
 \therefore \omega_{max} &= 34,000 \text{ cycles/sec}
 \end{aligned}$$

This maximum angular frequency can be used to estimate the maximum Strouhal number using the following relations.

$$\begin{aligned}\omega_{max} &= 2\pi f_{max} \\ \therefore f_{max} &= \frac{\omega_{max}}{2\pi} \\ \therefore f_{max} &= 5,411 \text{ Hz}\end{aligned}$$

From this maximum frequency, the non-dimensionalized Strouhal number can be calculated. The Strouhal number non-dimensionalizes frequency by using the jet exit diameter and the exit velocity.

$$\begin{aligned}St_{max} &= \frac{f_{max} * d_e}{V_{exit}} \\ \therefore St_{max} &= \frac{5411 \text{ Hz} \times 0.0275 \text{ m}}{427.5 \text{ m/s}} \\ \therefore St_{max} &= 0.348\end{aligned}$$

From the above calculations, it is seen that the maximum Strouhal number that can be resolved is approximately 0.348. This lies at approximately the third peak to be resolved. Therefore, it is concluded that the mesh resolution is sufficient to resolve the acoustics required.

2.5.3 Azimuthal Requirements

An important source of jet noise is the contributions from the helical modes of the jet. These helical modes are created by flow in the azimuthal direction of the jet. Helical modes are numbered by the number of wavelengths that are found around all 360° of the jet. These modes are numbered according to the number of wavelengths. For example, mode 1 contains one entire wavelength, mode 2 contains two entire wavelengths and so on. The most crucial modes in order of their contribution to jet noise are mode 1, mode 0 and mode 2. A quick check is done to ensure that at least these three modes are completely resolved in the simulation.

For the 90° mesh, there are 37 grid points in the azimuthal direction. This corresponds to 148 points around all 360°. As discussed in the previous subsection, the minimum number of points required to resolve a wavelength are 8. Therefore, the number of wavelengths (modes)

which are resolved is the quotient of dividing the number of points by 8. This calculation leads to solution that 18 modes are resolved in this simulation. This is more than enough to resolve the important modes relevant to noise.

2.6 Physical models and Boundary Conditions

Air is modeled as a single species gas. The density is calculated using the ideal gas formulation after each iteration. This relation is shown in equation 2.6.

$$p = \rho RT \quad (2.6)$$

The viscosity is calculated as a function of temperature using Sutherland's viscosity law using the three coefficient method. This relation is shown in equation 2.7

$$\mu = \lambda \frac{T^{3/2}}{T + C} \quad (2.7)$$

where λ is a constant for a gas and is given by equation 2.8.

$$\lambda = \frac{\mu_0(T_0 + C)}{T_0^{3/2}} \quad (2.8)$$

where μ is the dynamic viscosity at temperature T , μ_0 is the reference viscosity at reference temperature T_0 and C is the Sutherland's constant for the gas. For air, C is 270 K, T_0 is 291.15 K, μ_0 is 18.27 $\mu\text{Pa}\cdot\text{s}$ and λ is 1.512041288 $\mu\text{Pa}\cdot\text{s}\cdot\text{K}^{-1/2}$.

ANSYS FLUENT contains a number of boundary conditions that can be used for different surfaces. Before defining boundary conditions, the operating condition for pressure was set to 0 Pa. This makes all pressures referenced to 0 Pa, or all pressures input or output are absolute pressures. This is the recommended setting for any supersonic flow.

The nozzle inlet is modeled as a pressure inlet. This boundary condition is recommended for supersonic inlets, especially where there might be stagnation zones close the nozzle. The total pressure and temperature at the inlet is given by the experimental setup. To calculate the supersonic/initial gauge pressure, isentropic relations are used as given in equation 2.9. Turbulence was prescribed at the inlet using turbulent intensity and hydraulic diameter. This is the option recommended by the FLUENT documentation when dealing with fully developed internal flows. The turbulent intensity was set to 2% and the hydraulic diameter was set to 0.127 m.

$$p = p_0 \left(1 + \frac{\gamma - 1}{2} M^2 \right)^{\gamma-1/\gamma} \quad (2.9)$$

The pressure outlet boundary condition was used for the far-field. The static pressure and total temperature were maintained at ambient conditions. The turbulence parameters prescribed at the far field are back flow turbulent intensity and back flow turbulent viscosity ratio. The turbulent intensity was set to 1% and the turbulent viscosity was set to 2. All solid surfaces were modeled as walls. The walls are fixed, no slip, adiabatic (zero heat flux) surfaces. All boundary conditions are summarized in table 2.3.

Table 2.3: Summary of boundary conditions used

Region	Boundary Condition	Inputs
Inlet	Pressure inlet	Stagnation pressure Static pressure Stagnation temperature Turbulent intensity Hydraulic diameter
Far-field	Pressure outlet	Static pressure Stagnation temperature Turbulent intensity Turbulent viscosity ratio
Nozzle, lift plate, ground plate	Wall	No slip No heat flux

2.7 Ffowcs Williams-Hawkings Acoustics Integral Surface

The Ffowcs Williams and Hawkings (FW-H) [7, 16] equation is an inhomogeneous wave equation derived by manipulating the continuity equation and the Navier-Stokes equations. It can be written as:

$$\frac{1}{a_0^2} \frac{\partial^2 p'}{\partial t^2} - \nabla^2 p' = \frac{\partial^2 (T_{ij} H(f))}{\partial x_i \partial x_j} - \frac{\partial}{\partial x_i} \{ [P_{ij} n_i + \rho u_i (u_n - v_n)] \delta(f) \} + \frac{\partial}{\partial t} \{ [\rho_0 v_n + \rho (u_n - v_n)] \delta(f) \} \quad (2.10)$$

where p' is the sound pressure at the far field ($p' = p - p_0$). $f = 0$ denotes a mathematical surface introduced to ‘embed’ the exterior flow problem ($f > 0$) in an unbounded space, which facilitates the use of generalized function theory and the free-space Green function to obtain the solution. The surface ($f = 0$) corresponds to the source (emission) surface, and can be made coincident with a body (impermeable) surface or a permeable surface off the

body surface. n_i is the unit normal vector pointing toward the exterior region ($f > 0$) and T_{ij} is the Lighthill stress tensor defined as,

$$T_{ij} = \rho u_i u_j + P_{ij} - a_0^2(\rho - \rho_0)\delta_{ij} \quad (2.11)$$

P_{ij} is the compressive stress tensor. For a Stokesian fluid, it is given by,

$$P_{ij} = p\delta_{ij} - \mu \left[\frac{\partial u_i}{\partial x_j} + \frac{\partial u_j}{\partial x_i} - \frac{2}{3} \frac{\partial u_k}{\partial x_k} \delta_{ij} \right] \quad (2.12)$$

The free-stream quantities are denoted by the subscript 0. The wave equation 2.10 can be integrated analytically under the assumptions of the free-space flow and the absence of obstacles between the sound sources and the receivers. The complete solution consists of surface integrals and volume integrals. The surface integrals represent the contributions from all sources inside the acoustic surface, whereas the volume integrals represent quadrupole sources in the region outside the acoustic surface. It should be noted that when the surface is not permeable then the first term becomes the monopole sources (thickness noise p_T) and the second term is the dipole sources (loading noise p_L). The contribution of the volume integrals becomes small when the flow is low subsonic. When this term is taken to be zero we are assuming that the acoustic surface encloses all the sources. In ANSYS FLUENT, the volume integrals are dropped, and the solution becomes,

$$p'(\mathbf{x}, t) = p'_T(\mathbf{x}, t) + p'_L(\mathbf{x}, t) \quad (2.13)$$

$$4\pi p'_T(\mathbf{x}, t) = \int_{f=0} \left[\frac{\rho_0(\dot{U}_n + U_{\dot{n}})}{r(1 - M_r)^2} \right] dS + \int_{f=0} \left[\frac{\rho_0 U_n \left\{ r\dot{M}_r + a_0(M_r - M^2) \right\}}{r^2(1 - M_r)^3} \right] dS \quad (2.14)$$

$$\begin{aligned} 4\pi p'_L(\mathbf{x}, t) &= \frac{1}{a_0} \int_{f=0} \left[\frac{\dot{L}_r}{r(1 - M_r)^2} \right] dS + \int_{f=0} \left[\frac{L_r - L_M}{r^2(1 - M_r)^2} \right] dS \\ &+ \frac{1}{a_0} \int_{f=0} \left[\frac{L_r \left\{ r\dot{M}_r + a_0(M_r - M^2) \right\}}{r^2(1 - M_r)^3} \right] dS \end{aligned} \quad (2.15)$$

where,

$$U_i = v_i + \frac{\rho}{\rho_0}(u_i - v_i) \quad L_i = P_{ij}\hat{n}_j + \rho u_i(u_n - v_n) \quad (2.16)$$

The square brackets in Equations 2.14 and 2.15 denote that the kernels of the integrals are computed at the corresponding retarded times, τ , defined as follows, given the receiver time, t and the distance to the receiver, r ,

$$\tau = t - \frac{r}{a_0} \quad (2.17)$$

The various subscripted quantities appearing in Equations 2.14 and 2.15 are the inner products of a vector and a unit vector implied by the subscript. E.g., $L_r = \mathbf{L} \cdot \mathbf{r} = L_r r_i$, and $U_n = \mathbf{U} \cdot \mathbf{n} = u_i n_i$, where \mathbf{r} and \mathbf{n} denote the unit vectors in the radiation and wall-normal directions, respectively. The Mach number vector M_i in Equations 2.14 and 2.15 relates to the motion of the integration surface: $M_i = \frac{v_i}{a_0}$. The L_i quantity is a scalar product $L_i M_i$. The dot over a variable denotes source-time differentiation of that variable.

The formulation permits the source surface $f = 0$ to be permeable, and therefore can be placed in the interior of the flow. In this simulation, a cylindrical surface concentric with the jet core, with a radius of 10 throat diameters was set as the FW-H surface as can be seen in figure 2.3. This placement was selected since no major discontinuities or turbulent structures intersect the surface at this location. This was also eventually verified by viewing contours of the vorticity magnitude. The placement of this FW-H surface is recommended in the research of supersonic impinging jets by Erwin and Sinha [6].

There are a number of key advantages to using a FW-H surface as compared to directly measuring acoustic pressures at an observer location. Firstly, once the data is stored on the FW-H surface, it can be used to calculate sound data at any observer location outside the surface ($f > 0$). This means that multiple observers can be set up using the same simulation data. The other advantage of using this method is that the grid resolution does not need to be fine enough to resolve acoustics all the way to the observer location, but only inside the surface ($f < 0$). Therefore, the computational mesh can be much more computationally efficient, especially if the observer is located very far from the source region or outside the computational domain.

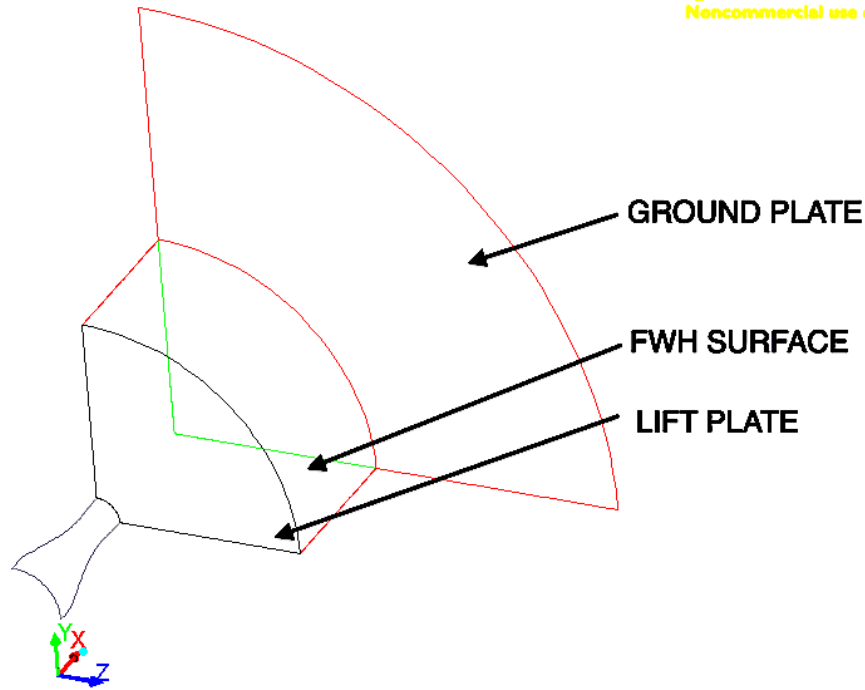


Figure 2.3: Location of FW-H Surface

2.8 Acoustics Post-Processing

To obtain an accurate frequency analysis of the noise spectrum, adequate sampling of the test data is necessary. The minimum number of samples required is calculated based on the minimum frequency of the required resolvable spectrum. On studying the experimental data, it was seen that the minimum resolvable frequency needs to be approximately 1,000 Hz, which is lower than the first actual peak. The minimum sample length required to resolve this frequency was calculated to be 400 using equation 2.18. This was multiplied by a factor of safety of 10, as recommended by Mendez et al. [19], to give 4,000 samples.

$$f_{\min} = \frac{1}{N\Delta t} \quad (2.18)$$

Chapter 3

Results

The results from the simulation were studied in four different aspects. Firstly, the flow behavior and structure was studied to ensure that the flow was fully developed and passed all sanity checks. Next, the mean centerline flow field was studied and compared with experimental data. The next step was to study the acoustics by estimating the sound sources and viewing the normalized pressure propagation. Finally, the acoustic spectra at the microphone was studied and compared with experimental data.

3.1 Flow Behavior

As discussed, the simulation went through a series of steps: FMG initialization, RANS solution and DDES. It is interesting to note the development of the flow field within each of these steps. Figures 3.1 to 3.4 show the contour plots of the flow after carrying out the full multi-grid initialization. On studying the contours of pressure (figure 3.1) and Mach number (figure 3.1), it can be seen that a number of important flow characteristics are already starting to be resolved. Most importantly, the jet exit Mach number is correctly resolved to 1.5 and the stagnation zone is created as expected. However, some of the flow features are not resolved at all, specifically the turbulence parameters. This can be seen most clearly in the contour plot of turbulent kinetic energy (figure 3.4).

Figures 3.5 to 3.8 show the contour plots after the RANS simulation. It is important to note here that the RANS simulation was not carried out all the way to perfect convergence, since it is only a setup step before DDES. The RANS simulation results show a better resolution of the flow features. From the pressure contour plot in figure 3.5 it can be seen that the jet core region and the stagnation region are better resolved, and match better with published experimental results. From the plot of Mach number in figure 3.6, the development of the wall jet can be seen clearly. The stagnation region and the stand-off shock right before

the stagnation zone are also resolved. Most importantly, basic turbulence features are better resolved as can be seen in the TKE plot (figure 3.8). The turbulence seen is a result of the development of the shear layer as well as the high turbulence in the wall jet region. It is important to note no quantitative analysis is done using RANS data since not all the turbulent structures are fully developed. However, the RANS flow field is used to estimate the basic flow behavior.

Finally, figures 3.9 to 3.12 show instantaneous contours for the DDES simulation.

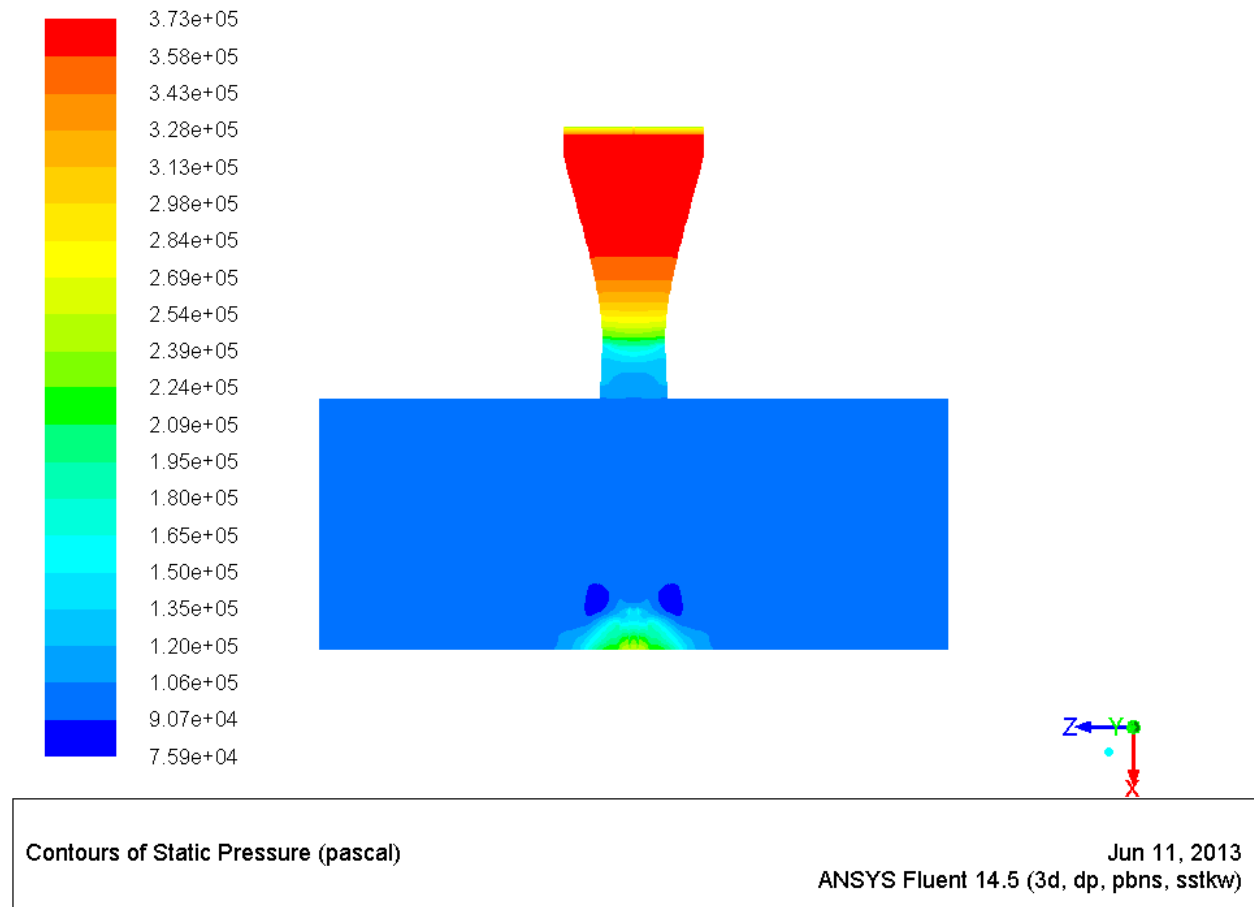


Figure 3.1: Static pressure contours after full multi-grid initialization

To fully understand the dynamics of the solution, an animation of the Mach number is important to view. This animation verifies that the flow propagates in the expected directions. Time histories of Mach number are shown in figure 3.13. A few dynamic flow features can be seen clearly from these plots. Firstly, the end of the potential core can be seen to be fluctuating. This means that the stagnation zone is not constant, but in a continuous state of motion. Next, the dynamics of the wall jet (flow parallel to the wall away from the jet core) can also be seen. It is noticed that this wall jet has a large circulation and high

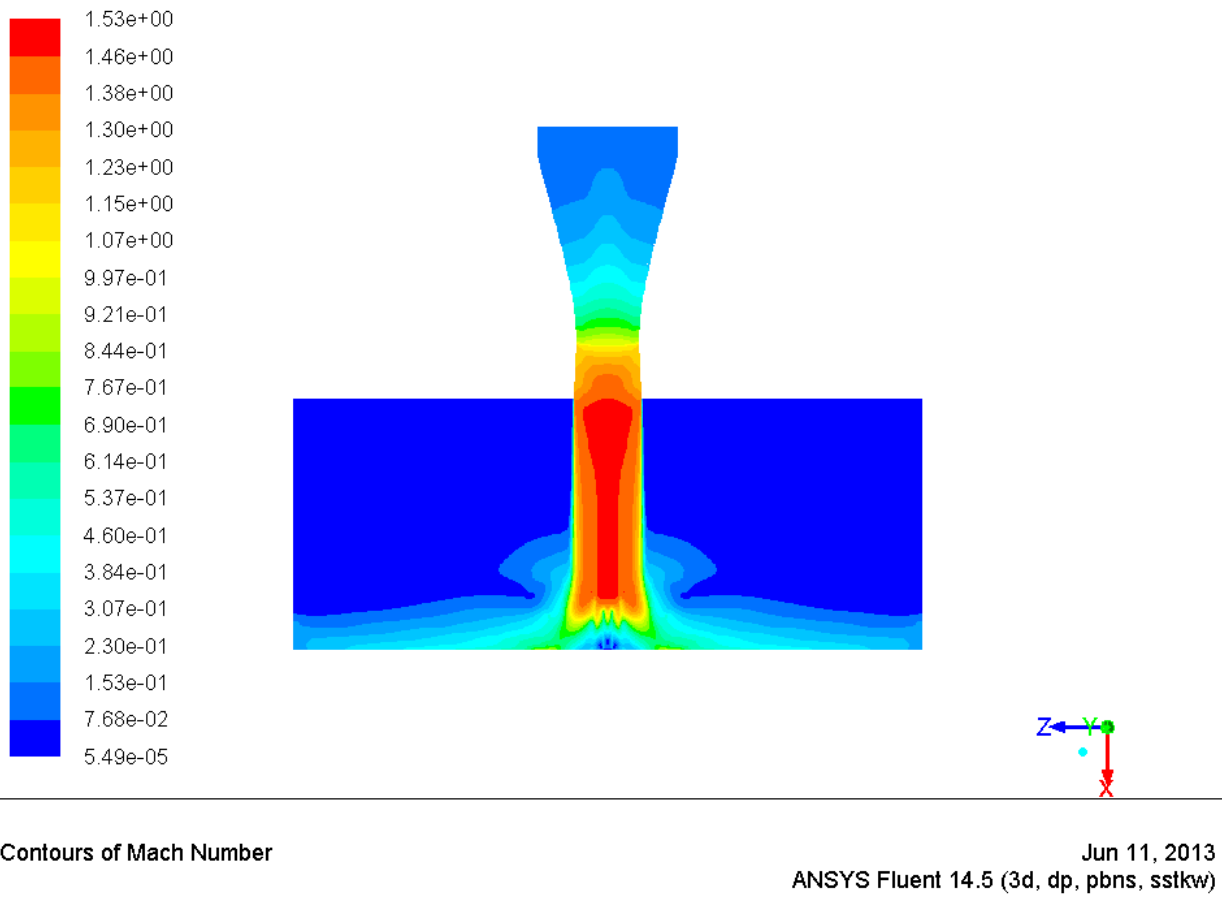


Figure 3.2: Mach number contours after full multi-grid initialization

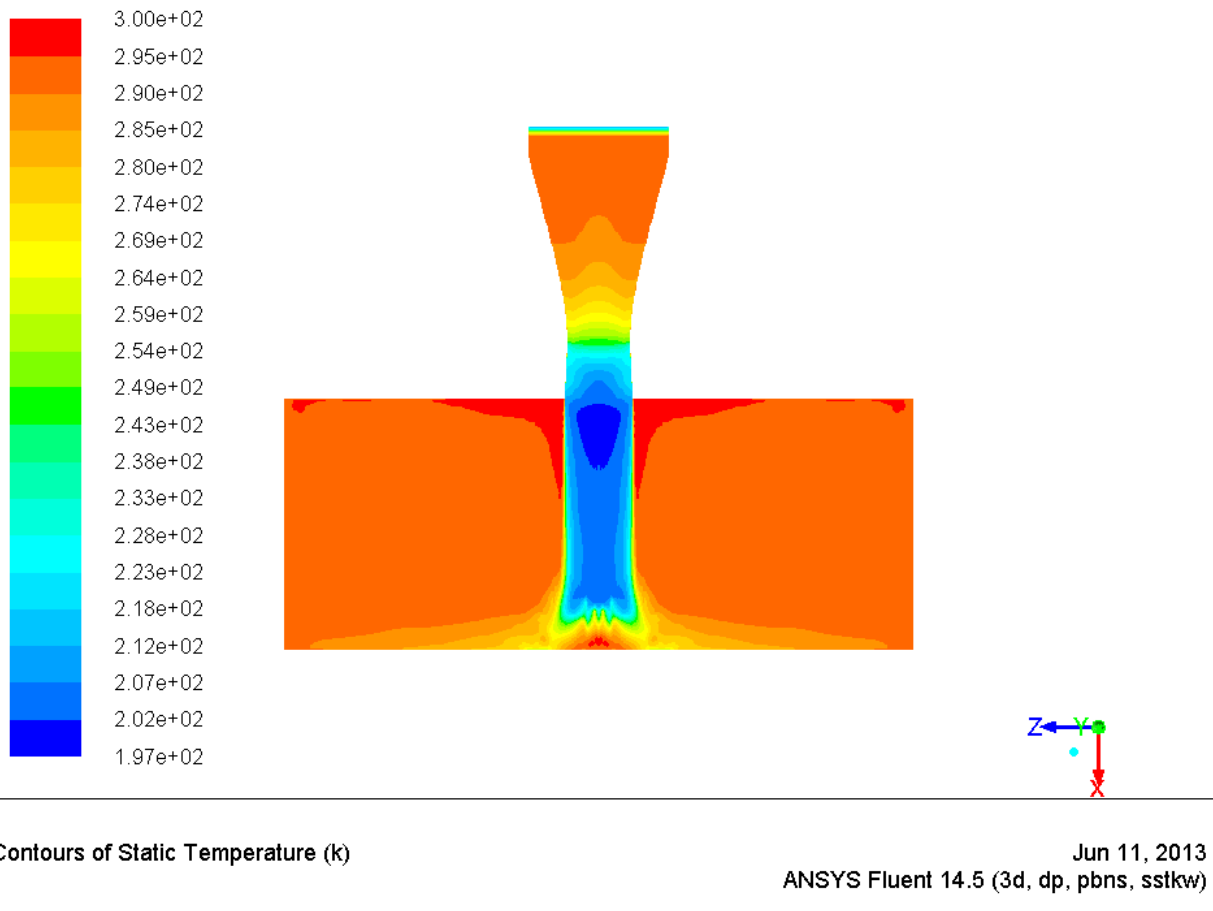


Figure 3.3: Static temperature contours after full multi-grid initialization

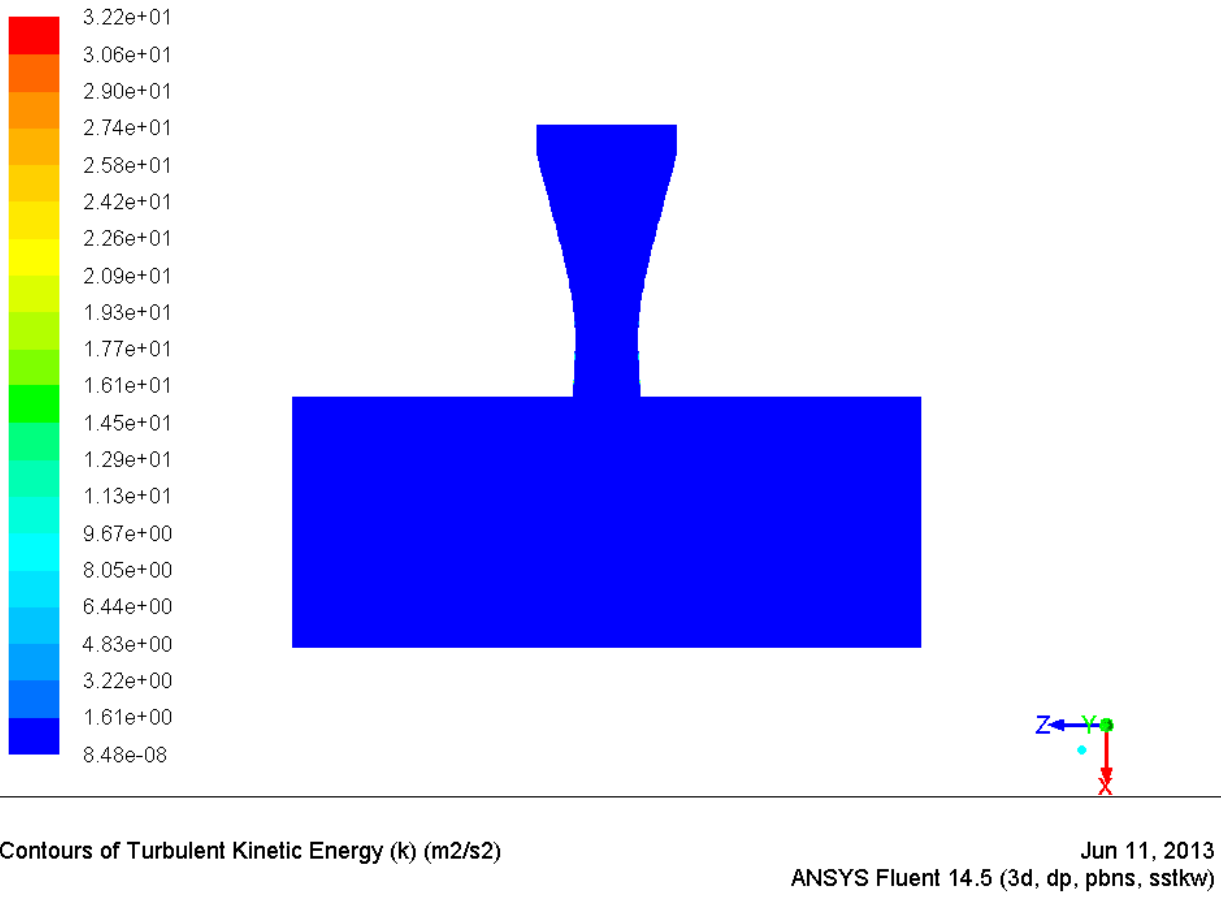


Figure 3.4: TKE contours after full multi-grid initialization

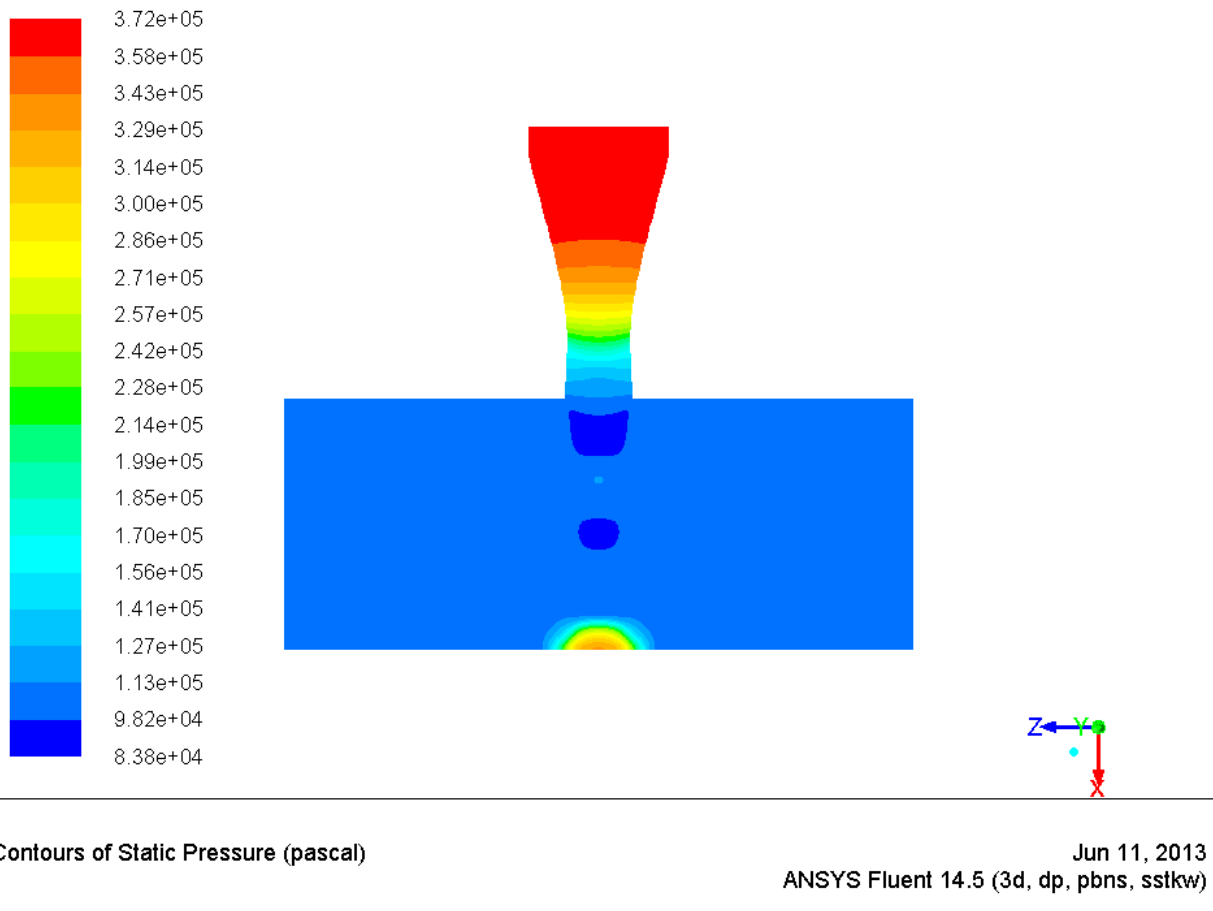


Figure 3.5: Static pressure contours after RANS simulation

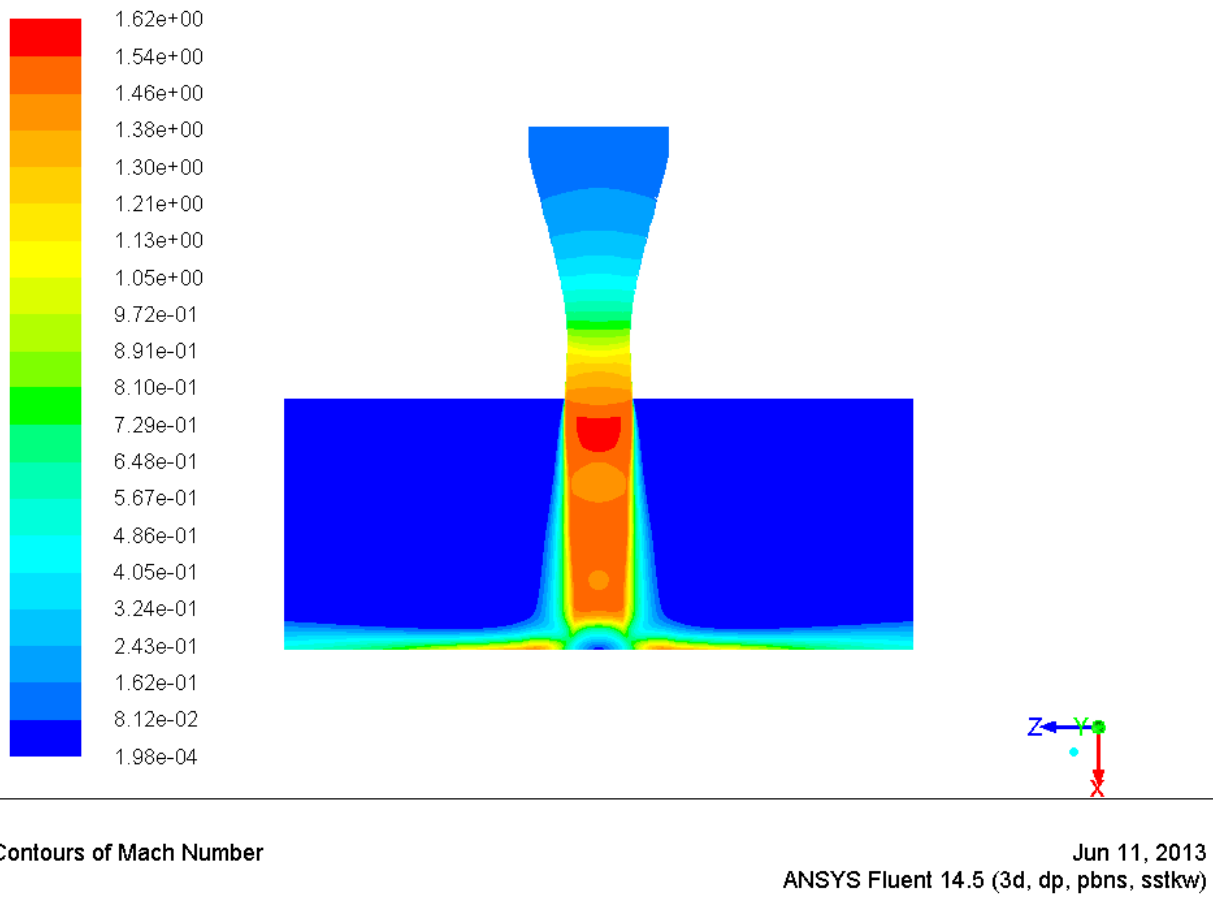
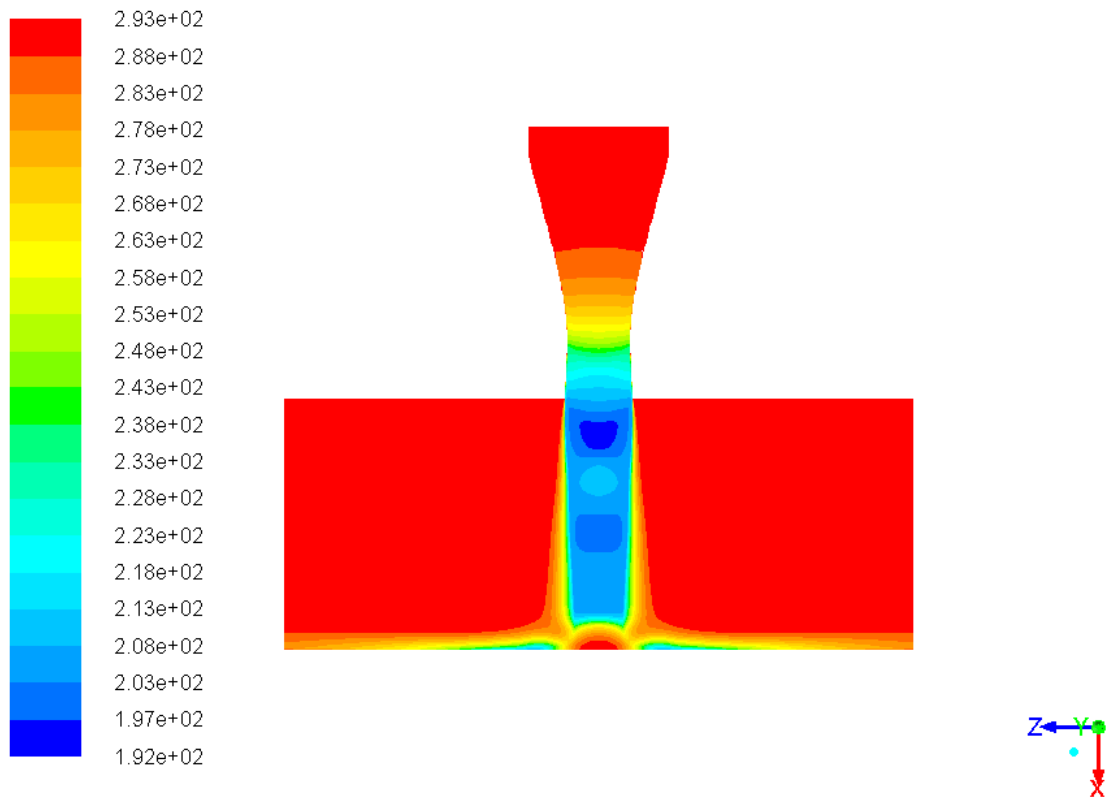


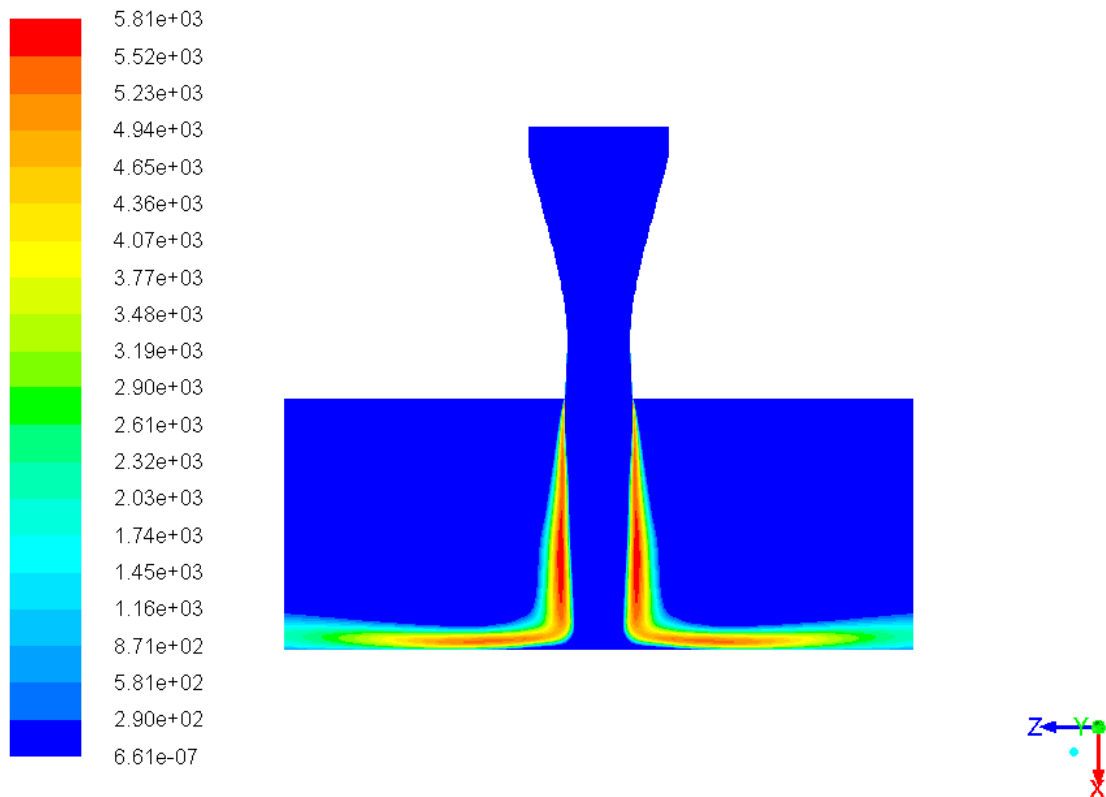
Figure 3.6: Mach number contours after RANS simulation



Contours of Static Temperature (k)

Jun 11, 2013
ANSYS Fluent 14.5 (3d, dp, pbns, sstk)

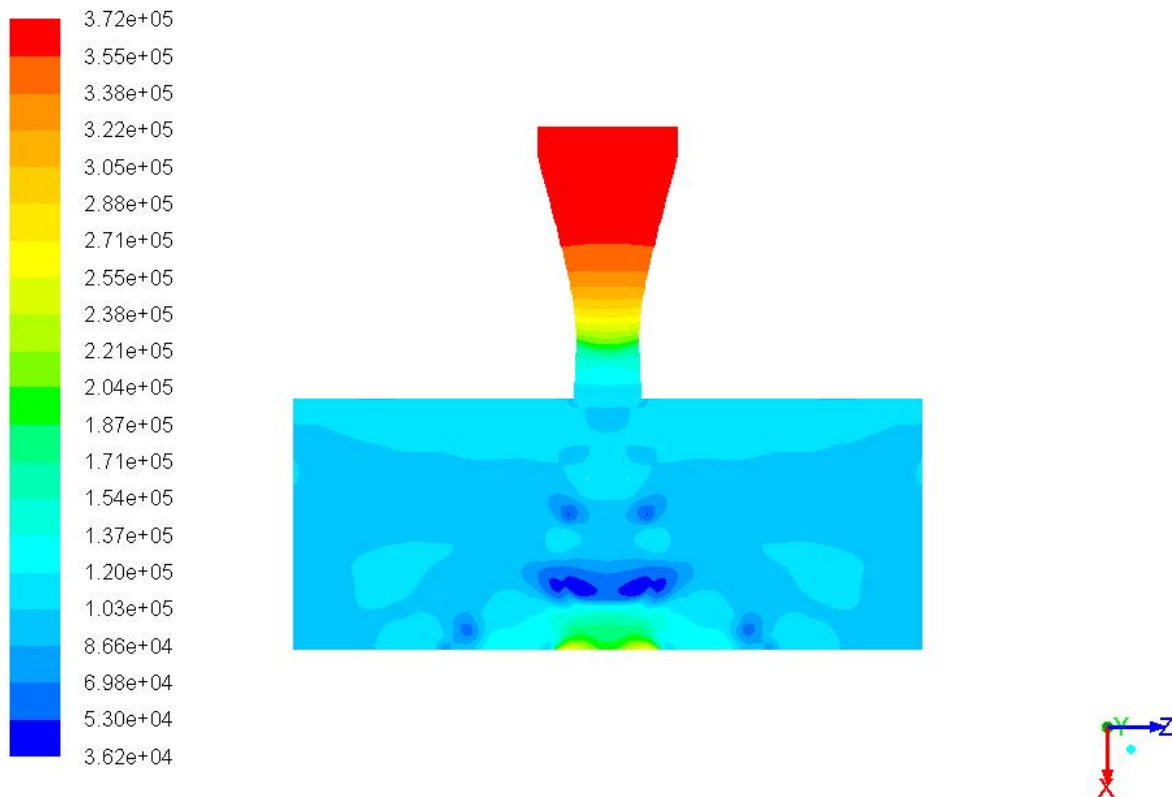
Figure 3.7: Static temperature contours after RANS simulation



Contours of Turbulent Kinetic Energy (k) (m2/s2)

Jun 11, 2013
 ANSYS Fluent 14.5 (3d, dp, pbns, sstk)

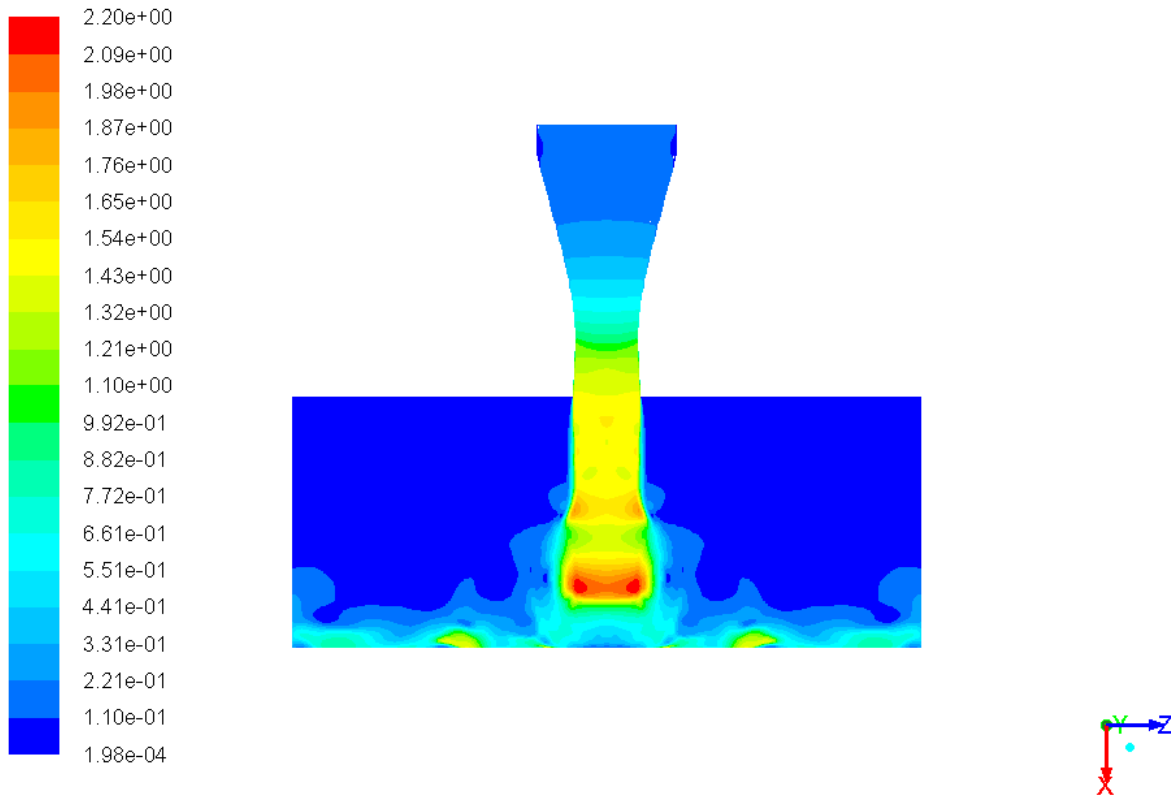
Figure 3.8: TKE contours after RANS simulation



Contours of Static Pressure (pascal) (Time=1.2500e-02)

Jun 11, 2013
 ANSYS Fluent 14.5 (3d, dp, pbns, DES, transient)

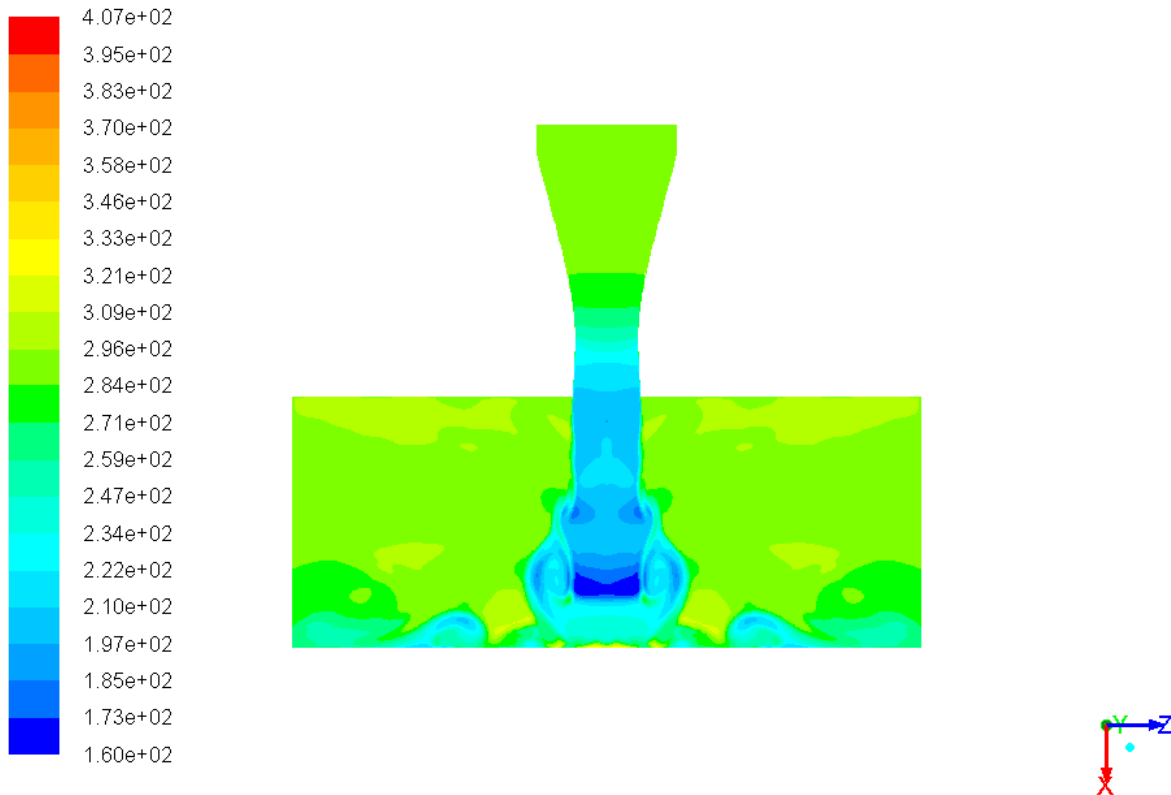
Figure 3.9: Static pressure contours after DDES simulation



Contours of Mach Number (Time= 1.2500×10^{-2})

Jun 11, 2013
ANSYS Fluent 14.5 (3d, dp, pbns, DES, transient)

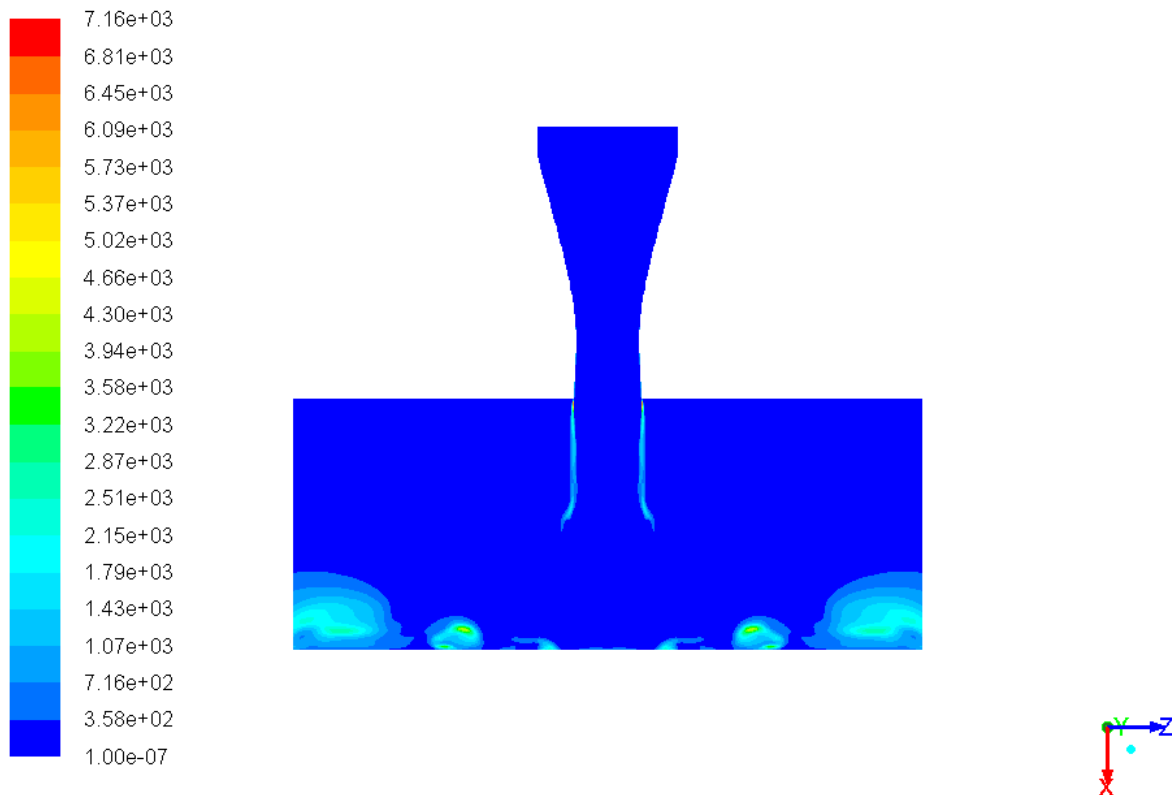
Figure 3.10: Mach number contours after DDES simulation



Contours of Static Temperature (k) (Time=1.2500e-02)

Jun 11, 2013
ANSYS Fluent 14.5 (3d, dp, pbns, DES, transient)

Figure 3.11: Static temperature contours after DDES simulation



Contours of Turbulent Kinetic Energy (k) (m2/s2) (Time=1.2500e-02)

Jun 11, 2013

ANSYS Fluent 14.5 (3d, dp, pbns, DES, transient)

Figure 3.12: TKE contours after DDES simulation

vorticity is expected in this region. This vortical structure seen in the wall jet is the main reason a high grid resolution was chosen for this part of the computational mesh.

All contour plots shown in this section pass a basic sanity check and provide all the expected flow features. These plots also compare well with the experimental data.

3.2 Mean Flow Field

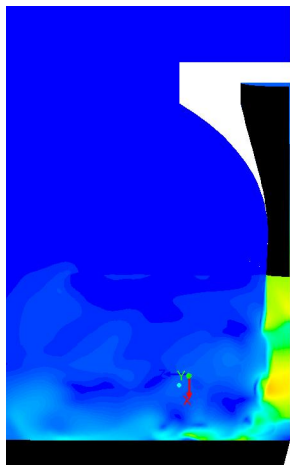
The next step in a structured validation is to compare some basic flow field data. In this case, the experimental data provided is centerline data. All simulation mean centerline data is time averaged DDES data for maximum accuracy. To non-dimensionalize the centerline to jet exit velocity, the jet exit velocity must first be calculated in the units of m/s. From section 3.1, it was validated that the jet exit Mach number is indeed 1.5 as expected. To calculate what exit velocity should be expected, the local speed of sound at the jet exit must be calculated. Using the jet stagnation temperature of 20°C and exit Mach number of 1.5, the static temperature can first be calculated to be 202.7 K using the isentropic relation shown in equation 3.1. Next, the local speed of sound at the jet exit was calculated to be 285.1 m/s using equation 3.2. Finally, the jet exit velocity was calculated to be 428 m/s using equation 3.3.

$$T = T_0 \left[1 + \left(\frac{\gamma - 1}{2} \right) M_j^2 \right]^{-1} \quad (3.1)$$

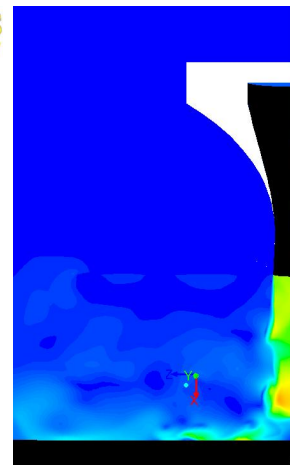
$$a = \sqrt{\gamma R T} \quad (3.2)$$

$$v_{exit} = M_j a \quad (3.3)$$

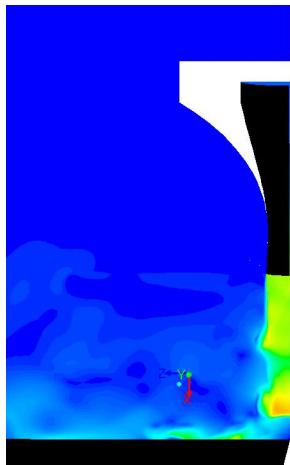
Figure 3.14 shows the comparison of simulation centerline velocity with experimental data. It can be seen that there is good comparison between simulation and experimental data. The major difference between simulation and experimental data is the location of the end of the potential core. Experimental data suggests that the potential core end at approximately 3 throat diameters from the jet exit while simulation data predicts the potential core ends at approximately 3.5 throat diameters from the jet exit. However, this difference is within an acceptable range. It is speculated that the major cause for this difference is the fact that some of the turbulence parameters specified for the jet inlet are only approximates of the experimental conditions. Keeping this in mind, it was concluded that the mean centerline flow field of the jet compares well with experimental data.



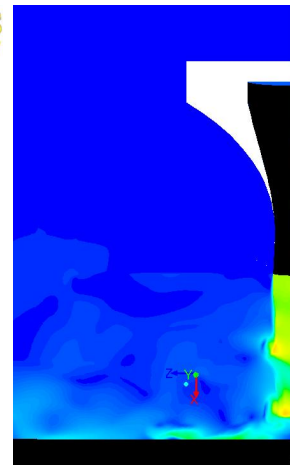
(a)



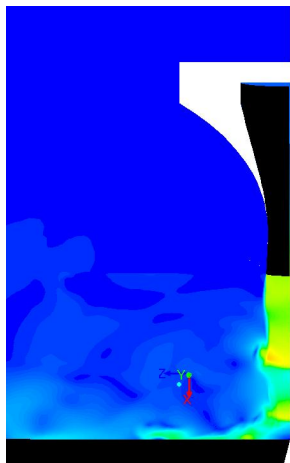
(b)



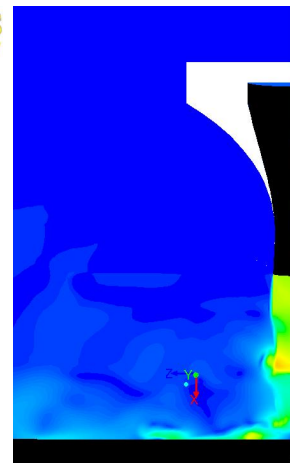
(c)



(d)



(e)



(f)

Figure 3.13: Instantaneous Mach number contours. Each successive figure represents the next time step

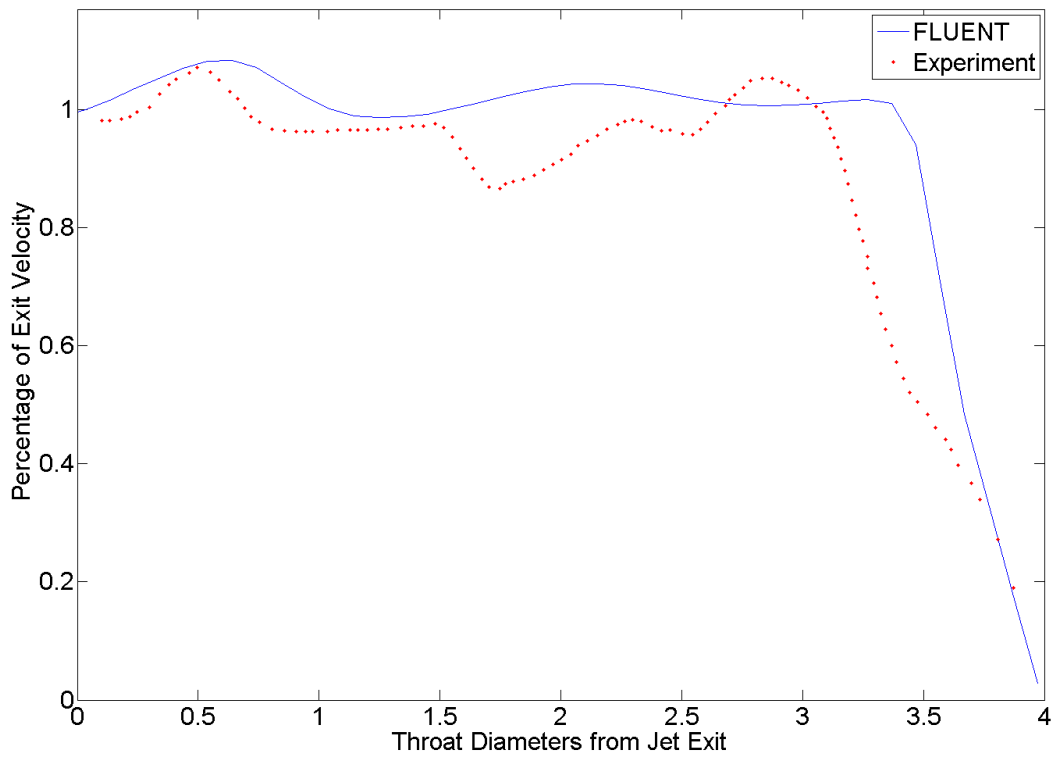


Figure 3.14: Centerline Velocity of the Jet

3.3 Acoustics

3.3.1 Sound Source Identification

Identifying the sound sources in the given simulation is important for future simulations and ultimately, for noise mitigation purposes. Since the acoustics source surface requires that all acoustics containing features must be included within the surface, a preliminary estimation of the sound sources can be useful. Additionally, once the sound sources are identified, efforts can be made to change the flow features most related to the sound produced by changing various parameters.

An estimate of the sound sources can be made by studying the vorticity magnitude contour plot (shown in figure 3.15). Some of the major sources of sound are the shear layer of the jet, the wall jet and the region of the shear layer close to the end of the potential core.

The vertical black lines in the plot denote the location of acoustics source surface. It can be seen that some small vortical structures are seen intersecting the surface. This feature is compounded by the fact that the mesh is stretched out right after the acoustics surface. Therefore, there might be additional vortical structures outside the acoustics surface which are not resolved by the stretched mesh. This indicates that some of the sound producing structures are not completely contained within the acoustics source surface. This means that not all sound will be captured by the surface, leading to an under prediction.

3.3.2 Feedback Mechanism

Before quantifying the acoustic spectra, the feedback mechanism responsible for the distinct tones was examined. As previously mentioned in chapter 1, this feedback mechanism leads to oscillations in the jet which correspond to high amplitude discrete tones. This feedback is started by the pressure waves that reflect off the impingement surface which propagate upstream to interact with the lip of the nozzle exit. This interaction then leads to further excitation of the shear layer and certain oscillations to appear in the jet. These oscillations also give rise to the periodicity of the wall jet. Finally, these oscillations also affect the stability of the normal standoff shock right before the stagnation bubble. This shock movement is also a major source of noise. The frequency of this jet oscillation is set at the stable feedback frequency of the waves propagating upstream and the shear layer excitation.

The best way to visualize acoustic pressure waves is to examine the contour plots of normalized pressure. Normalized pressure is the ratio between the local static pressure and the ambient atmospheric pressure (1 atm in this case). Small pressure fluctuations in the flow field are seen as 'ripples' which are in turn representative of the acoustic waves generated.

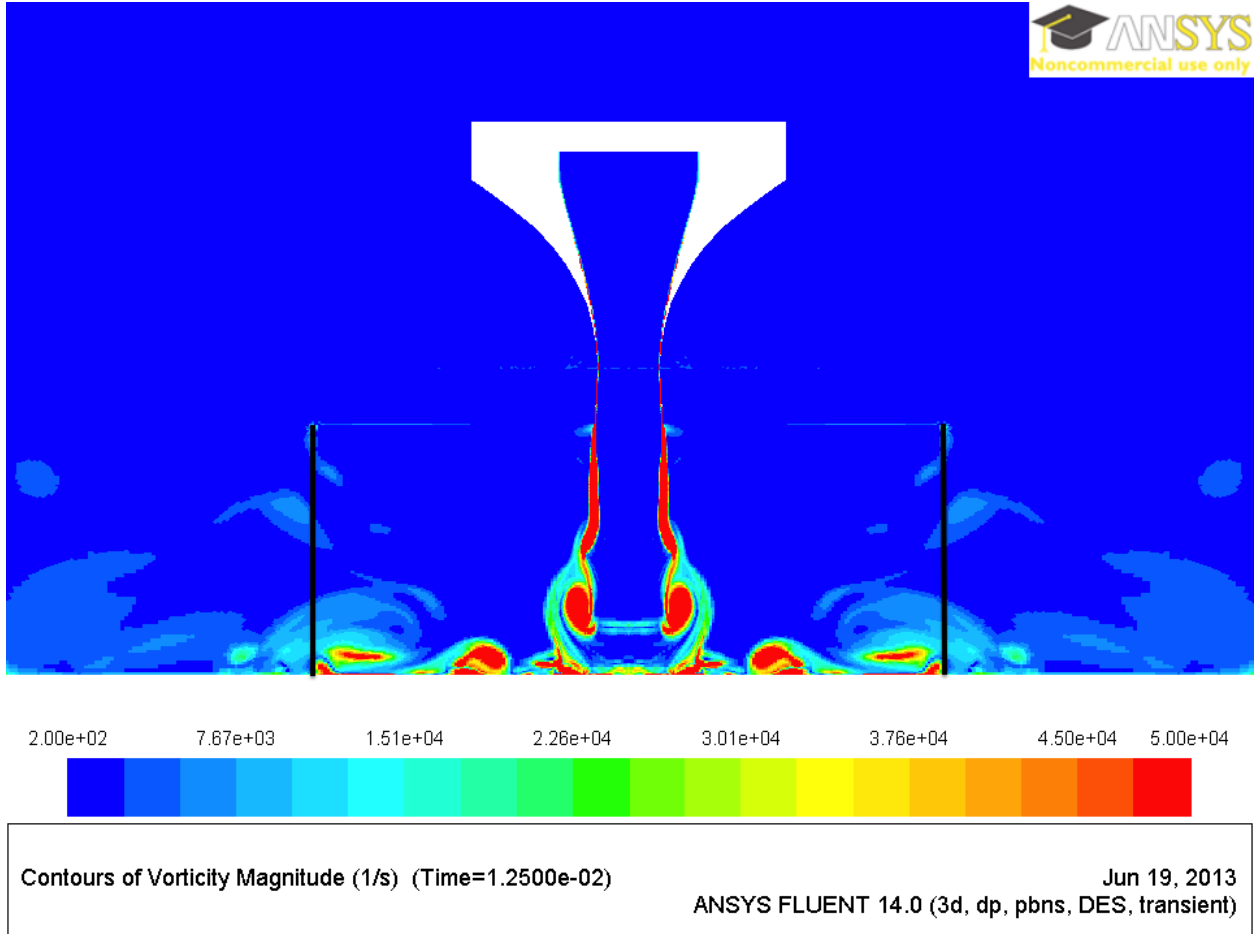


Figure 3.15: Instantaneous vorticity magnitude contour plot

The development of this feedback mechanism is illustrated in figure 3.16 which shows certain snapshots of normalized pressure. As expected, the first acoustic waves that reflect off the wall interact with the nozzle lip to further excite the shear layer. The actual oscillations of the jet can be seen in figure 3.13 and figure 3.17. It is noted that certain structures develop within the jet at a certain frequency. Inspection of the Mach number contours also shows the

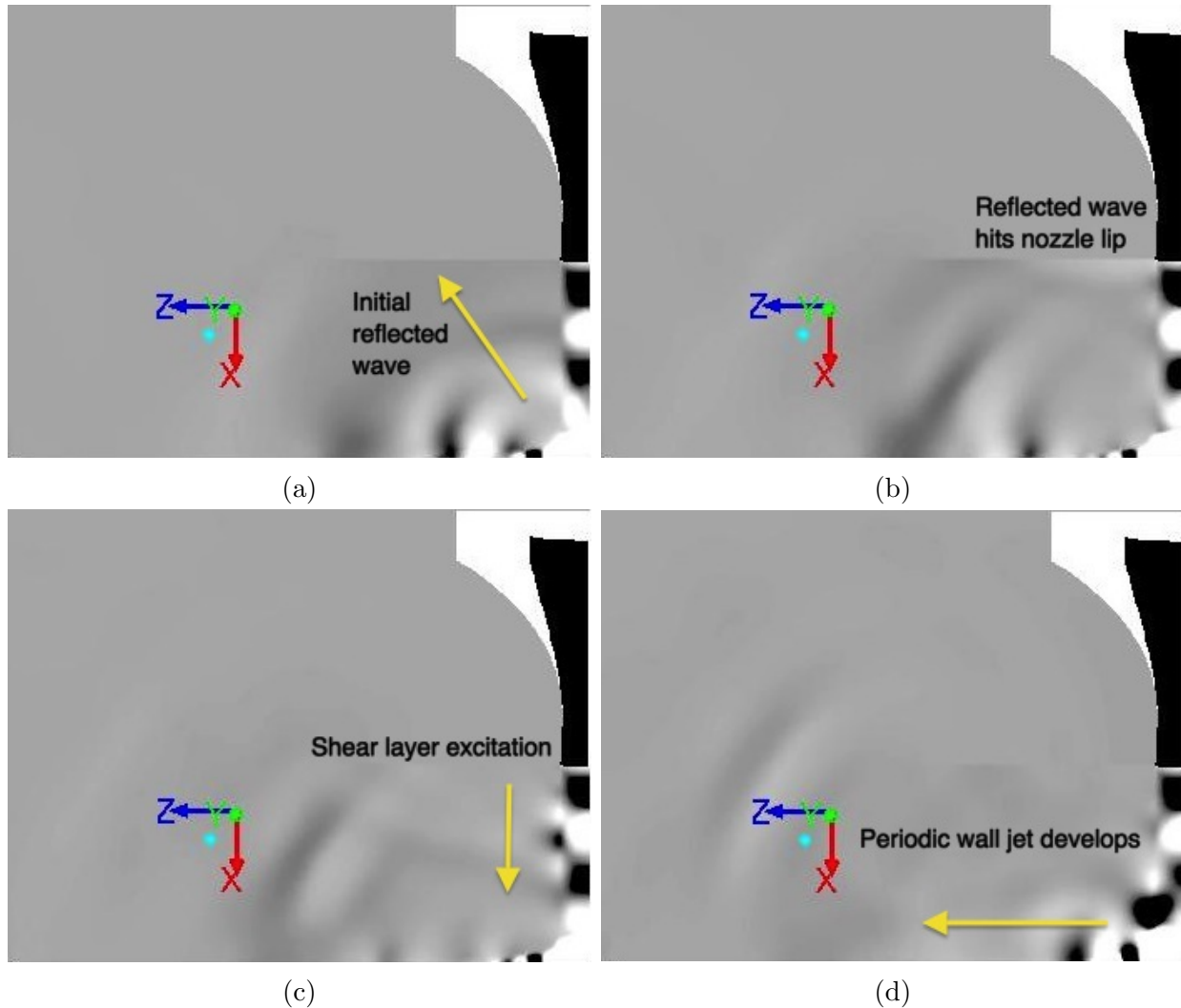


Figure 3.16: Normalized pressure contours demonstrating development of the feedback mechanism

3.3.3 Near-Field Measurements

To qualitatively validate how that the acoustics are being propagated in the domain, snapshots of the normalized pressure must be seen once the flow is completely developed. Viewing

an animation of the normalized pressure contours basically provides an understanding about the direction of propagation of acoustics. Snapshots of the normalized pressure contours in time are shown in figure 3.17.

A closer look into figure 3.17 shows that these pressure waves propagate away from the impingement region at a specific angle. This angle is a first indication of the directivity of the noise produced. One of the major things that can be inferred from the normalized pressure contours is the absence of reflections from the boundaries of the domain. These reflections can be a major concern for most acoustics simulations and it must be confirmed that no far-field reflections occur to ensure the simulation is of adequate quality. Therefore, it was concluded that the far-field was stretched sufficiently for the simulation.

To conduct a quantitative analysis of the acoustics produced, the acoustic spectra was studied. To do this, the time histories of acoustic pressure were first recorded at the microphone location. To just extract the fluctuations in the pressure (which is the source of acoustics), the mean pressure level was first calculated from the pressure time history and subtracted from each data point. This data was then put through a Fast-Fourier Transform (FFT) algorithm to convert all the data from the time domain to the frequency domain. Equation 3.4 is used to convert all sound pressure level (SPL) data to decibel scale.

$$\text{SPL [dB]} = 20 \log_{10} \frac{p_{\text{rms}}}{p_{\text{ref}}} \quad (3.4)$$

where p_{rms} is the root mean square pressure and p_{ref} is the reference acoustic pressure. In this case, p_{ref} is 2E-5 Pa.

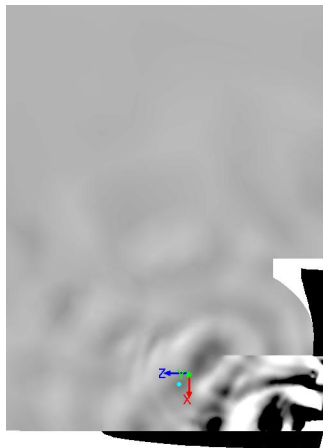
All frequencies in this section are non-dimensionalized to Strouhal number using the jet exit velocity and the nozzle throat diameter as shown in equation 3.5. When studying the acoustic spectra, it should be kept in mind that the high frequency portion of the spectra is just numerical noise. In this region, it appears that the spectra experiences a sudden drop off of amplitude. This is due to the fact that the computational mesh cannot resolve such high frequencies. As shown in chapter 2, the maximum Strouhal number that can be resolved by the mesh is 0.35, which is past the peaks that are expected to be resolved. In this high Strouhal number region, the SPL drops off suddenly. Another important factor to keep in mind is that all acoustic spectra showed in this report are narrow band spectra, i.e., there is no octave banding. This is to ensure that there is similarity when comparing simulation data to experimental data. This lack of octave banding is the reason for the high frequency of the jaggedness. However, the high amplitude for the jagged fluctuations of the spectra are currently not accounted for. It is speculated that using an averaging technique like Bartlett's technique will smooth out the high amplitude jaggedness.



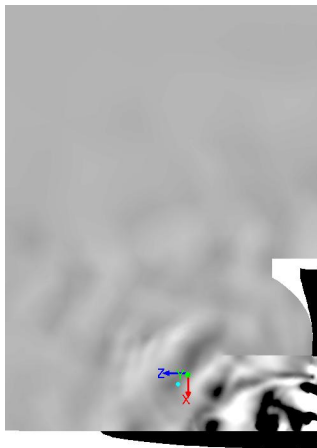
(a)



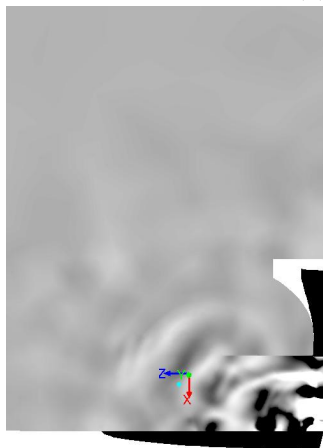
(b)



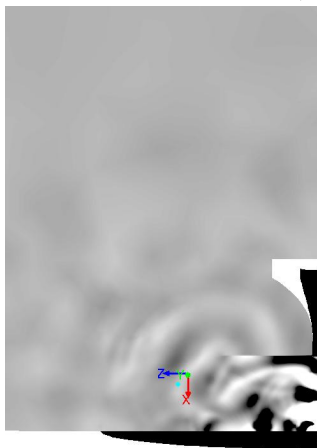
(c)



(d)



(e)



(f)



Figure 3.17: Instantaneous Normalized Pressure Contours. Each successive figure represents the next time step.

$$St = \frac{fd_t}{V_{\text{exit}}} \quad (3.5)$$

Figure 3.18 shows the acoustic spectra obtained from the simulation as compared to experimental data. The simulation data captures three dominant peaks seen in the experimental data. The Strouhal numbers of the peaks match up quite well. It can be seen that the first peak is over-predicted by FLUENT by approximately 10 dB. However, the next two peaks are predicted within a tolerance of 1 dB. The broadband level of the SPL spectrum also matches well with the experimental data.

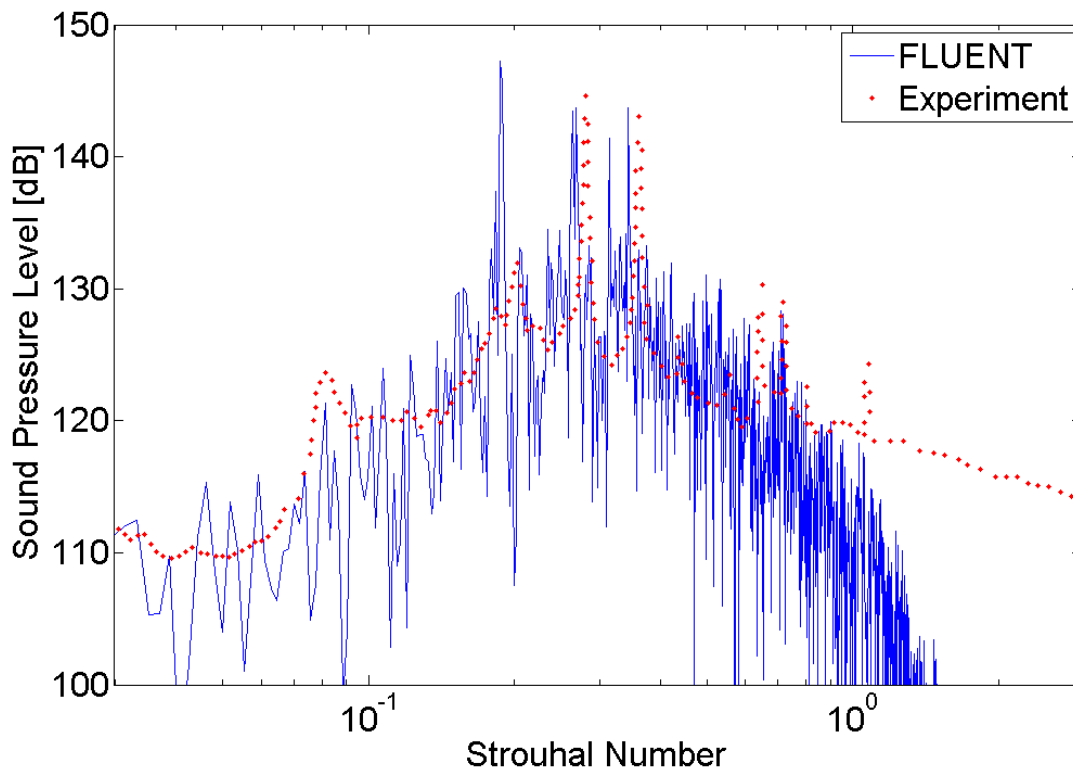


Figure 3.18: Comparison of simulation SPL data with experiment

3.3.4 Effect of quarter vs full nozzle mesh

Due to computational restrictions, the simulation was run for only a quarter section of the nozzle. For maximum accuracy, a full 360° mesh should be used. The quarter nozzle has some loss in accuracy due to a lack of complete turbulence that is generated as compared to a full mesh. The lack of turbulent structures directly relates to a lack in the sound pressure levels that are calculated. This is shown by the fact that helical modes are not fully

developed by using only a quarter section of the nozzle.

However, one single test case was run using the full 360° mesh and the resulting acoustic spectra is showed in figure 3.19. It can be seen that the three dominant peaks are predicted as well as the quarter nozzle case. Therefore, it is concluded that for the current accuracy level, a full 360° is not critical. A more computationally efficient 90° mesh is sufficient for capturing the vital features of the flow field.

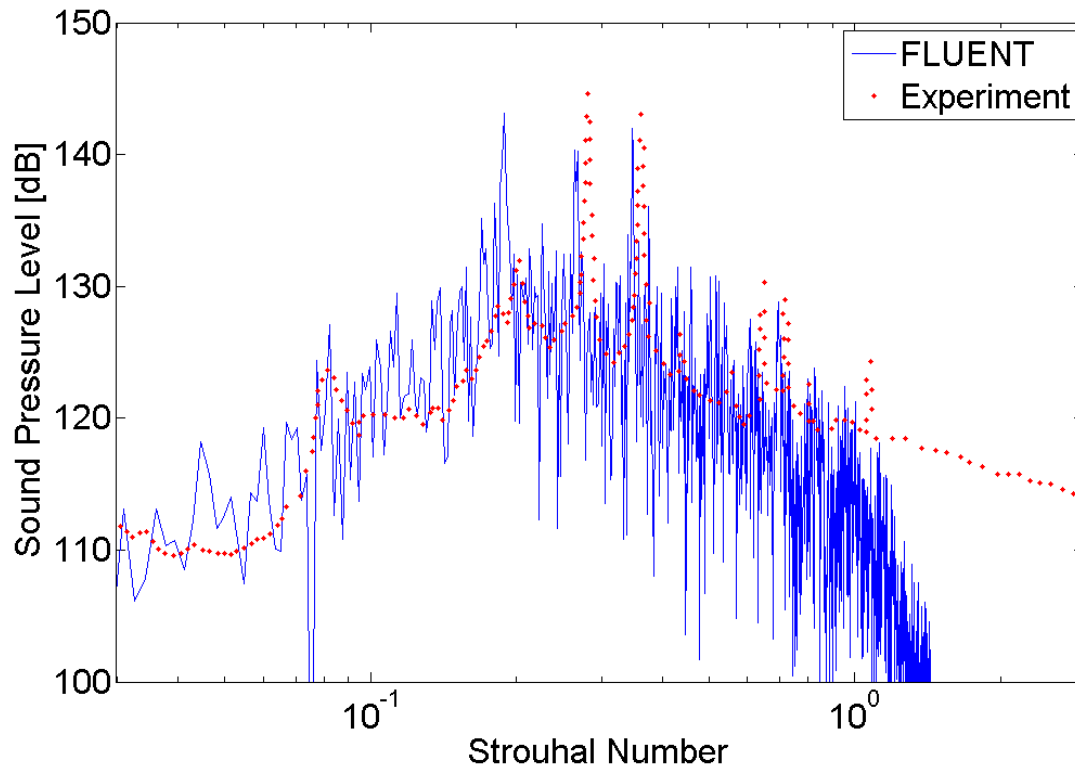


Figure 3.19: Comparison of simulation SPL data with experiment using the direct propagation method (360° mesh)

3.3.5 Ffowcs-Williams & Hawkings Results

The acoustics spectra was also calculated using the FWH acoustics surface method and is shown in figure 3.20. Similar to experimental data, three peaks are predicted by the FWH method. The Strouhal number of the peaks is also well predicted. However, there is a definite under prediction of amplitudes of the spectra, including the peaks and the broadband level. It is speculated that this under prediction is caused due to the following reasons:

1. As seen in figure 3.15, some of the sound sources of the case seem to be outside the

region enclosed by the FWH surface. This means that the SPL levels will be under-predicted since not all the sound sources are captured within the surface.

2. The FWH surface only gathers data for the quarter nozzle. The symmetry boundary conditions used do not compensate for the missing section of the nozzle when storing data on the acoustics surface. Even though the surface stores data for the quarter section of the nozzle closest to the microphone, and hence the most dominant quadrant, it misses contributions from other three quadrants of the jet. This leads to an under prediction in the SPL data.

As previously explained, the acoustic spectrum at a location is calculated as a post-processing step in the FW-H method. First, the microphone location was placed on top one of the symmetry planes. The resulting acoustic spectrum is shown in figure 3.20.

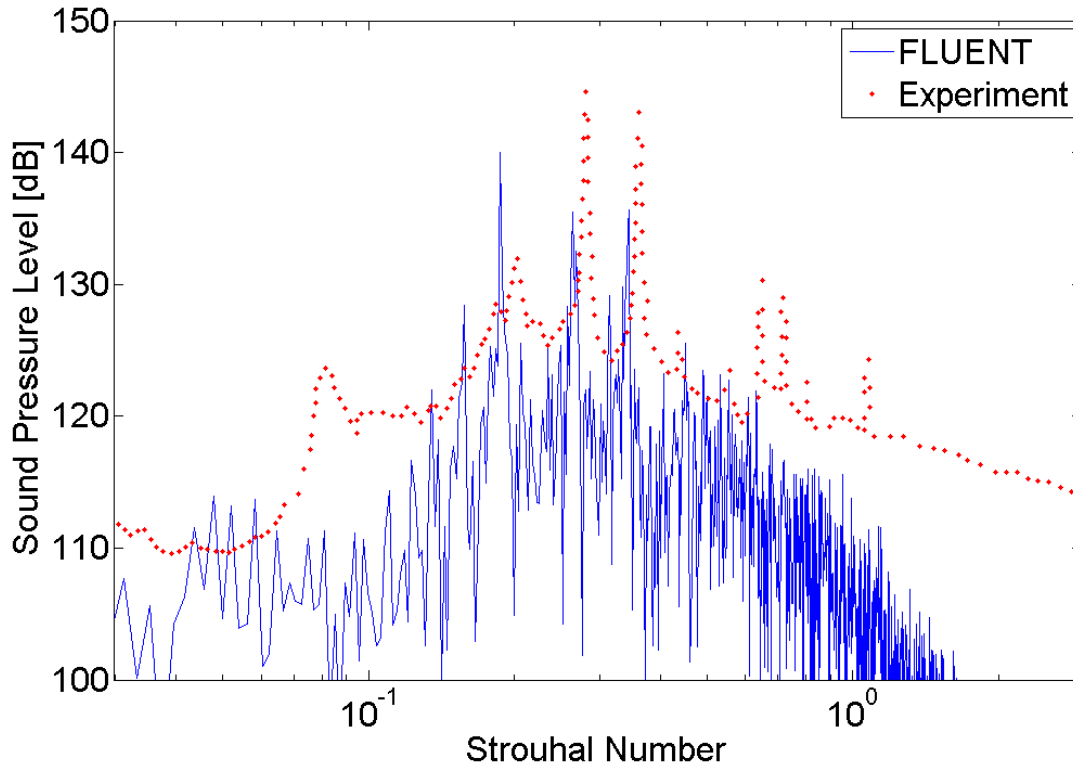


Figure 3.20: Comparison of simulation SPL data with experiment calculated using the FWH source surface

On examining figure 3.20, an under prediction of the sound pressure levels is observed. It was speculated that this is due to the fact that only one quadrant of the physical problem makes a contribution to acoustics due to the fact that only a quarter nozzle was modeled. Since the microphone was placed in plane with one of the symmetry planes, it was decided

that two quadrants can be accounted for by doubling the acoustic pressure history at the microphone. This would account for both of the dominant quadrants of the physical domain. The acoustic spectrum obtained as a result of this doubling is shown in figure 3.21.

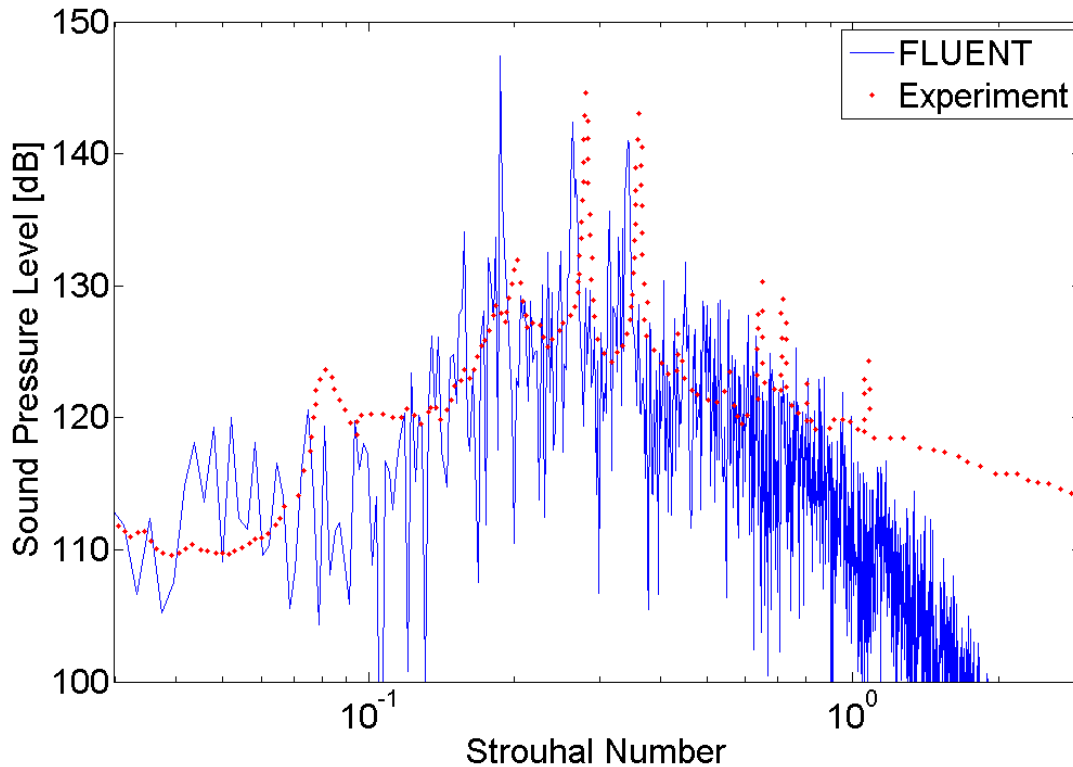


Figure 3.21: Comparison of simulation SPL data with experimental data on doubling acoustic pressure history calculated on symmetry plane

As expected, the sound pressure level is higher once the acoustic pressures are doubled. The final result is a much better comparison with experimental data. It was concluded that this was an improved and more accurate method of estimating acoustics.

Effect of Microphone Location

The placement of the microphone in plane with a symmetry plane potentially carries the risk of adding some noise to the acoustic data. This was of special importance for this study since the acoustic spectrum contains some jaggedness. To rule out the possibility of this inaccuracies, a case was run by placing the microphone in between both symmetry planes. The resulting acoustic spectrum is shown in figure 3.22.

On examining figure 3.22, it is noticed that the jaggedness in the spectrum is the same and there is no reduction in noise. This can be attributed to the fact that the collection

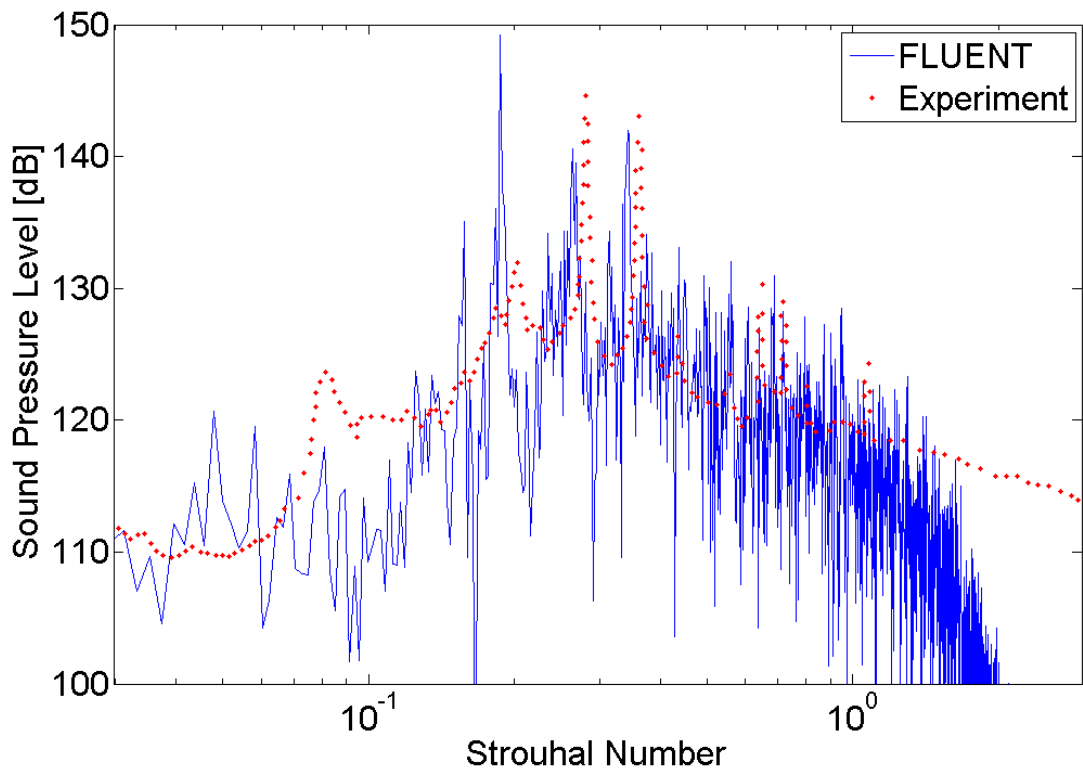


Figure 3.22: Comparison of simulation SPL data with experimental data with microphone location between both symmetry planes

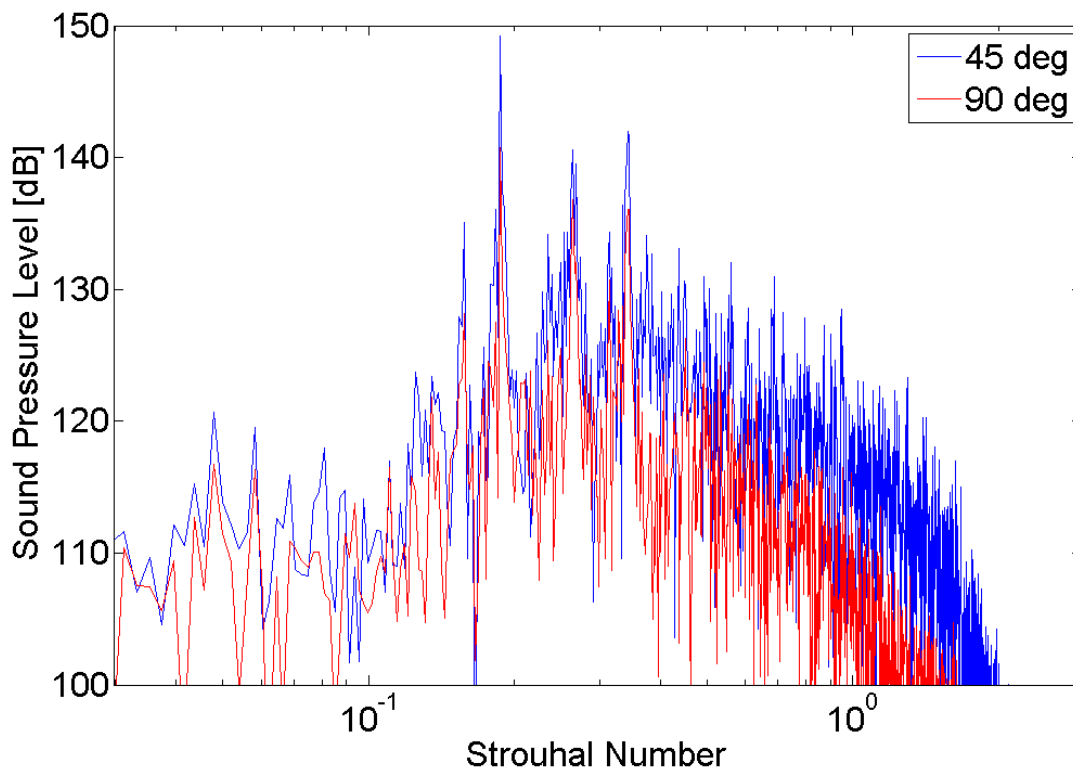


Figure 3.23: Comparison of simulation SPL data from both microphone location cases

of data on the FW-H surface is independent of microphone location, and the final sound pressure level is calculated analytically.

For a better understanding of how the trends changed, a direct comparison between the results calculated at both microphone locations is helpful. This comparison is shown in figure 3.23, where ‘45 deg’ refers to the case where the microphone is in between symmetry planes and ‘90 deg’ refers to the case where the microphone is on one of the symmetry planes. To ensure that an equal comparison is made, the results are made without doubling the acoustic pressure history, since this is not a valid assumption for the ‘45 deg’ case.

A discussion of better experimental correlation between the ‘45 deg’ and the ‘90 deg’ case cannot be done, since the ‘45 deg’ results cannot be directly doubled as is the case with the ‘90 deg’ case. It is already discussed that this doubling at the ‘90 deg’ case is the valid approach for quantitative comparisons.

3.3.6 Directivity

The directivity of the sound can be estimated by studying the Overall Sound Pressure Level (OASPL) at mics located at different angles from the jet axis. OASPL can be calculated

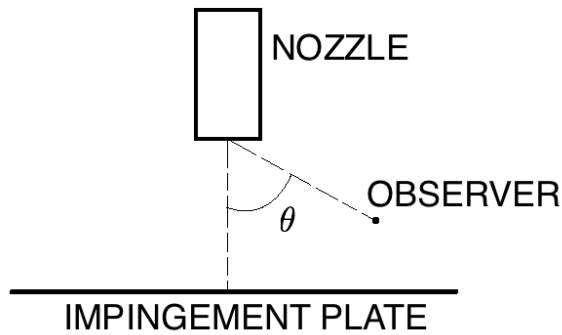


Figure 3.24: Angle calculation for directivity

by integrating the SPL spectrum over all frequencies. The SPL spectra for each mic was calculated by using the data stored on the acoustics source surface and then applying the FWH method. Even though the FWH method under predicts the amplitude of sound, it still provides good trends which can be used in estimating OASPL directivity. However, it becomes important to note that the OASPL levels will be under predicted. The angle for the directivity is calculated as shown in figure 3.24, which implies that the axial direction corresponds to 0° and the sideline direction corresponds to 90° . Multiple points are used in calculating the OASPL levels. These microphones are distributed in a circular arc with a radius of 25 cm. It is for this reason that the directivities are only calculated for angles greater than 70° , since anything below that lies past the impingement plate and is outside the computational domain. The directivity of the case is shown in figure 3.25. It is noticed that the directivity increases from 70° to 90° and then starts to drop off. This shows that the noise is loudest in the radial direction.

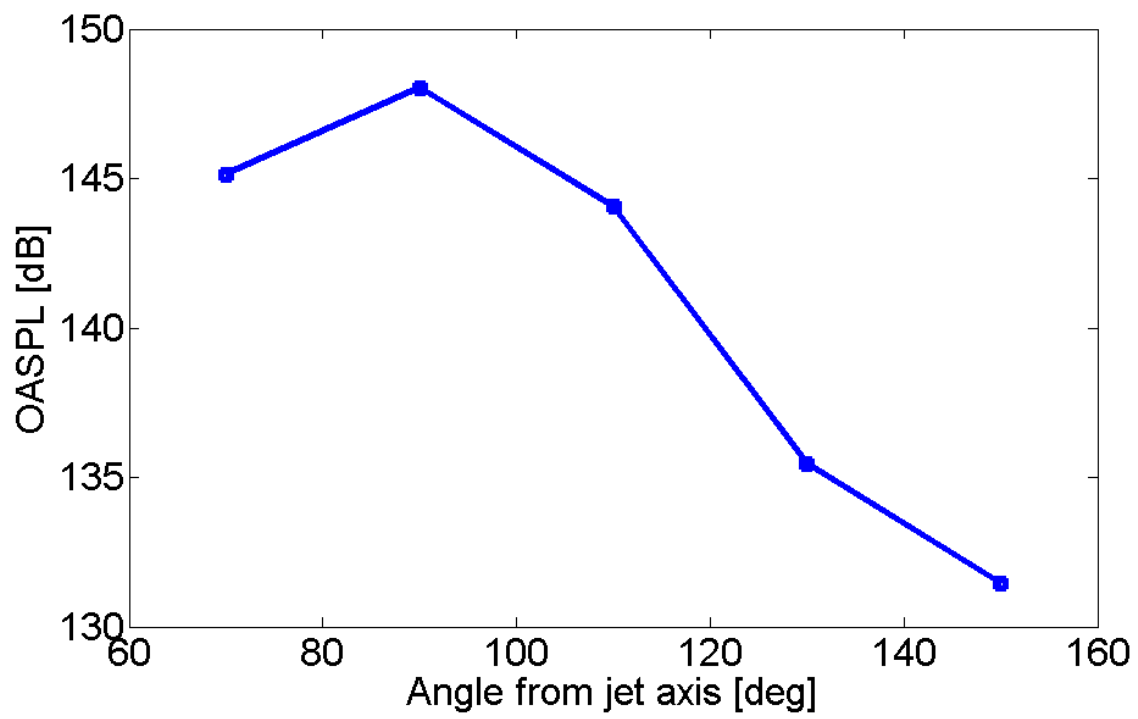


Figure 3.25: Directivity of the sound produced

Chapter 4

Conclusions and Future Work

A number of steps were taken to validate the ANSYS FLUENT code for studies relating to supersonic jet impingement on flat plates:

1. The flow field generated from the simulation was examined and the flow structure was analyzed. The flow behavior matched well with expected results and experimental data.
2. The mean flow field of the jet centerline was examined by comparing time averaged DDES measurements with experimental results. Simulation data matched well with experimental data.
3. The flow behavior relating to acoustics was analyzed. Pressure contours were studied to view the propagation of acoustic waves throughout the domain. No reflections from the boundaries were observed in the simulation and it was concluded that the far-field was stretched sufficiently. Acoustic spectra obtained at a microphone location was compared with experimental data and reasonable comparison was found. It was concluded that even using a relatively coarse computational grid of only a quarter nozzle, the acoustic spectra can be obtained for preliminary analysis. Results from a 90° nozzle mesh were compared to a 360° nozzle mesh and it was found that the acoustic spectra was defined well enough by just using a 90° mesh.
4. The FWH integral acoustics source method was successfully used to generate the acoustic spectra at the same microphone location. It was found that doubling the acoustics history when measured on the symmetry plane was an acceptable method for calculating the acoustics spectrum. This also implies that the sound is highly prevalent only in the two quadrants closest to the observer, and there is a high rate of decay. A slight

under prediction of amplitude can be attributed to the fact that not all the vortical structures (sound sources) were contained within the FW-H surface.

In addition, the flow was analyzed to verify the theory that a feedback mechanism is a major source of acoustics in supersonic impinging jets. It was shown that the pressure waves reflecting off the impingement surface propagate upstream to interact with the nozzle lip and excite the shear layer.

This thesis could serve as a basis for multiple improvements and parametric studies for the study of supersonic impinging jets. Given that the simulation was run mainly as a proof of concept, there are many improvements in the simulation that can be made for providing additional and more accurate results. A grid dependence study must be carried out to ensure that all flow features are resolved with a reasonable amount of accuracy. The new version of ANSYS FLUENT being released at the time of writing will incorporate the use of non-reflective boundary conditions with the pressure based coupled solver. These non-reflective boundary conditions can be incorporated to avoid the need for an extensive stretched far field. Doing this will reduce the number of grid points and decrease computational costs of running the simulation.

The issues regarding the under prediction of SPL levels using the FWH method can also be looked into. Firstly, the mesh resolution on the FWH surface can be increased to study its effect on the SPL. Next, a full 360° mesh should be run with a fully wrapped around FWH surface. This will ensure that contributions to noise from all four quadrants will be included when calculating SPL. Lastly, a study on the placement of the FWH surface should be carried out to ensure that the FWH surface is enclosing all sound sources.

To fully identify the sound sources, the Lighthill stresses should be analyzed on a contour plot. These Lighthill stresses are a direct indication of the regions where sound is produced. However, to calculate these stresses, only the fluctuating component of the velocity is to be isolated. Therefore, the simulation must save a time history of data saved throughout the near field region so that the mean values can be subtracted. This was currently not done due to computational and data storage limitations.

Once the simulation has been improved and all of the above issues have been addressed, a number of parametric studies should be undertaken for noise mitigation purposes. For example, the effect of various jet parameters like Mach number, stagnation temperature etc. on noise can be studied. Another example would be the effect of changing geometric parameters like impingement surface inclination, shape, etc. on noise. Since the aim of this study is to model rocket lift off and aircraft jets, multi-phase simulations can be carried out with realistic rocket and aircraft jet gases to improve predictions for acoustics.

Bibliography

- [1] K. M. Aikens, A. S. Lyrintzis, and G. A. Blaisdell. Large eddy simulations of hot supersonic jets for aeroacoustics. Technical Report Navy STTR Phase II Final Report, Purdue University, February 2012.
- [2] ANSYS Inc., Canonsburg, PA. *Product Documentation Release 14.0*, 2010.
- [3] C. Bailly and S. Candel. Prediction of supersonic jet noise from a statistical acoustic model and a compressible turbulence closure. *Journal of Sound and Vibration*, 194(2):219, 242 1996.
- [4] M. R. Brown and A. Frendi. Supersonic jet impingement on a flat plate. In *Proceedings of the 33rd AIAA Aeroacoustics Conference*, Colorado Springs, CO, June 2012.
- [5] Y. Dewan, V. Golubev, A. Lyrintzis, R. Mankbadi, K. Kurbatskii, and E. Osman. Detached eddy simulations of supersonic jets impinging on flat plates. Number AIAA-2013-3097, June 2013.
- [6] J. P. Erwin, N. Sinha, and G. P. Rodebaugh. Large eddy simulation of supersonic impinging jets. *Journal of engineering for gas turbines and power*, 134(12), October 2012.
- [7] J. E. Ffowcs-Williams and D. L. Hawkings. Sound generation by turbulence and surfaces in arbitrary motion. *Philosophical Transactions of the Royal Society of London, Series A*, 264:321–342, 1969.
- [8] D. G. Holmes and S. D. Connell. Solution of the 2d navier-stokes equations on unstructured adaptive grids. *AIAA Paper 89-1392*.
- [9] B. R. Hutchinson and G. D. Raithby. A multigrid method based on the additive correction strategy. *Numerical Heat Transfer*, 9:511–537, 1986.
- [10] S. E. Kim, B. Makarov, and D. Caraeni. A multi-dimensional linear reconstruction scheme for arbitrary unstructured grids. *AIAA Paper 2003-3990*.

- [11] A. Krothapalli. Discrete tones generated by an impinging underexpanded rectangular jet. *AIAA Journal*, 23(12):1910–1915, 1985.
- [12] A. Krothapalli, E. Rajkuperan, F. Alvi, and L. Lourenco. Flow field and noise characteristics of a supersonic impinging jet. *Journal of Fluid Mechanics*, 392:155–181, 1999.
- [13] R. Kumar, S. Lazic, and F. S. Alvi. Control of high-temperature supersonic impinging jets using microjets. *AIAA Journal*, 47(12):2800–2811, December 2009.
- [14] Konstantin A. Kurbatskii. Scale-resolving simulation of an unsteady turbulent flow and acoustic field of a screeching supersonic jet. In *Proceedings of the 33rd AIAA Aeroacoustics Conference*, number AIAA 2012-2289, Colorado Springs, CO, June 2012.
- [15] B. P. Leonard. The ultimate conservative difference scheme applied to unsteady one-dimensional advection. *Computer Methods in Applied Mechanics and Engineering*, 88:17–74, 1991.
- [16] A. S. Lyrintzis. Integral acoustics methods: From the (cfd) near-field to the (acoustic) far-field. *International Journal of Aeroacoustics*, 2(2):95–128, 2003.
- [17] D. K. McLaughlin, G. L. Morrison, and T. R. Troutt. Experiments on the instability waves in a supersonic jet and their acoustic radiation. *Journal of Fluid Mechanics*, 69(1):73–95, 1975.
- [18] D. K. McLaughlin, G. L. Morrison, and T. R. Troutt. Reynolds number dependence on supersonic jet noise. *AIAA Journal*, 15(4):526–532, 1977.
- [19] S. Mendez, M. Shoeybi, A. Sharma, S. K. Lele, and P. Moin. Post-processing of large-eddy simulations for jet noise predictions. Annual research brieds, Center for Turbulence Research, 2009.
- [20] F. R. Menter and M. Kuntz. Adaptation of eddy-viscosity turbulence models to unsteady separated flow being vehicles. In *Proceedings of the Conference of Heavy Vehicles: Trucks, Busses and Trains*, Monterey, CA, 2002.
- [21] A. Powell. On the mechanism of choked jet noise. *Proceedings of the Physical Society of London*, B66:1039–1056, 1953.
- [22] A. Powell. On the noise emanating from a two-dimensional jet above the critical pressure. *American Quarterly*, 4:103–122, 1953.

- [23] G. Raman. Supersonic jet screech: half-century from powell to the present. *Journal of Sound and Vibration*, 225(3):543–571, 1999.
- [24] R. D. Rauch, J. T. Batira, and N. T. Y. Yang. Spatial adaption procedures on unstructured meshes for accurate unsteady aerodynamic flow computations. *AIAA Paper 91-1106*.
- [25] P. R. Spalart. Strategies for turbulence modelling and simulations. *International Journal of Heat and Fluid Flow*, 21:252–263, 2000.
- [26] P. R. Spalart, S. Deck, M. L. Shur, K. D. Squires, M. Strelets, and A. Travin. A new version of detached eddy simulation, resistant to ambiguous grid densities. *Journal of Theoretical and Computational Fluid Dynamics*, 20:181–195, 2006.
- [27] M. Strelets. Detached eddy simulation of massively separated flows. *AIAA Paper 2001-879*.
- [28] C. K. W. Tam and K. K. Ahuja. Theoretical model of discrete tone generation by impinging jets. *Journal of Fluid Mechanics*, 214:67–87, 1990.
- [29] S. P. Vanka. A calculation procedure for three-dimensional steady recirculating flows using multigrid methods. *Computer Methods in Applied Mechanics and Engineering*, 55:321–338, 1986.
- [30] S. Venkateswaran, J. M. Weiss, and C. L. Merkle. Propulsion related flow-fields using the preconditioned navier-stokes equations. In *Proceedings of the 28th AIAA/ASME/SAE/ASEE Joint Propulsion Conference*, number 92-3437, 1992.
- [31] J. M. Weiss and W. A. Smith. Preconditioning applied to variable and constant density flows. *AIAA Journal*, 33(11):2050–2057, 1995.